LETTER

doi:10.1038/nature14064

# Endophilin–A2 functions in membrane scission in clathrin-independent endocytosis

Henri-François Renard[1,2,3]*, Mijo Simunovic[4,5]*, Joël Lemière[6,7]*, Emmanuel Boucrot[8], Maria Daniela Garcia-Castillo[1,2,3], Senthil Arumugam[1,2,3], Valérie Chambon[1,2,3], Christophe Lamaze[2,3,9], Christian Wunder[1,2,3], Anne K. Kenworthy[10], Anne A. Schmidt[11], Harvey T. McMahon[12], Cécile Sykes[6]*, Patricia Bassereau[4]* & Ludger Johannes[1,2,3]

**During endocytosis, energy is invested to narrow the necks of cargo-containing plasma membrane invaginations to radii at which the opposing segments spontaneously coalesce, thereby leading to the detachment by scission of endocytic uptake carriers[1]. In the clathrin pathway, dynamin uses mechanical energy from GTP hydrolysis to this effect[2–4], assisted by the BIN/amphiphysin/Rvs (BAR) domain-containing protein endophilin[5,6]. Clathrin-independent endocytic events are often less reliant on dynamin[7], and whether in these cases BAR domain proteins such as endophilin contribute to scission has remained unexplored. Here we show, in human and other mammalian cell lines, that endophilin-A2 (endoA2) specifically and functionally associates with very early uptake structures that are induced by the bacterial Shiga and cholera toxins, which are both clathrin-independent endocytic cargoes[8]. In controlled *in vitro* systems, endoA2 reshapes membranes before scission. Furthermore, we demonstrate that endoA2, dynamin and actin contribute in parallel to the scission of Shiga-toxin-induced tubules. Our results establish a novel function of endoA2 in clathrin-independent endocytosis. They document that distinct scission factors operate in an additive manner, and predict that specificity within a given uptake process arises from defined combinations of universal modules. Our findings highlight a previously unnoticed link between membrane scaffolding by endoA2 and pulling-force-driven dynamic scission.**

Shiga toxin induces the clathrin-independent formation of endocytic plasma membrane invaginations as a first step in its entry into cells[8]. How this highly bent membrane domain is recognized by cellular machinery has remained unexplored. Here we screened an expression library of curvature-recognizing BAR domain proteins[9] for their localization to these structures. The screen was performed using the receptor-binding B-subunit of Shiga toxin (STxB) on cells with decreased levels of ATP to perturb active cellular machinery that is involved in the processing of these endocytic structures[8,10]. Out of 17 different BAR proteins, only Toca-1, Toca-3 and amphiphysin-2 scored positively (Extended Data Fig. 1a, yellow underlay). However, their short interfering RNA (siRNA)-mediated depletion did not affect STxB trafficking, hence these proteins were not studied further. In cells that expressed exogenous endoA2 (Extended Data Fig. 1a, green underlay), STxB-induced tubules were much shorter (Extended Data Fig. 1b), suggesting a functional crosstalk between endoA2 and the STxB uptake process. Because in non-ATP-depleted cells STxB trafficking to the Golgi was not detectably altered by expression of green fluorescent protein (GFP)-tagged endoA2 (Extended Data Fig. 1c), short tubules were probably the consequence of scission of longer tubules, rather than the inhibition of tubule formation.

At the plasma membrane and in very early uptake structures, STxB colocalized with endogenous endoA2 (Fig. 1a, b) or GFP–endoA2 (Fig. 1c, Extended Data Fig. 2a and Supplementary Video 1). Similar colocalization with endogenous endoA2 was observed for the GM1 glycosphingolipid-binding B-subunit of cholera toxin (CTxB) (Fig. 1a), which shares with STxB many aspects related to endocytic membrane bending[11]. Furthermore, the lifetime of structures containing endoA2 strongly increased in the presence of STxB (Extended Data Fig. 2b), and endoA2 was recruited

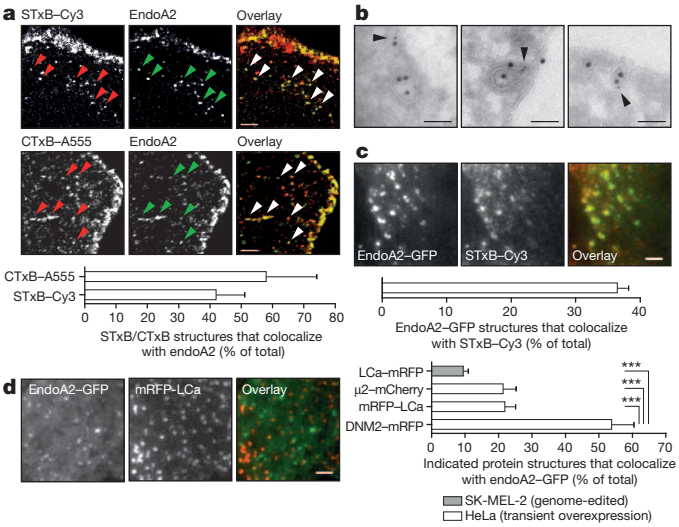


**Figure 1 | EndoA2 localization to endocytic pathways.** All conditions: incubation for 5 min at 37 °C (unless stated otherwise). **a**, BSC-1 cells with 50 nM STxB–Cy3 ($n = 20$ cells) or 5 nM CTxB-Alexa555 (A555) ($n = 50$ cells) for 3 min at 37 °C, and labelling for endoA2 (three independent experiments). **b**, Cryo-electron microscopy (representative of 50 images) on HeLa cells incubated with 0.5 μM STxB. Immunogold labelling: STxB, 15 nm gold particles; endoA2, 10 nm gold particles (arrowheads). **c**, HeLa cells transiently expressing endoA2–GFP incubated with 0.5 μM STxB–Cy3 and analysed by total internal reflection fluorescence microscopy (TIRFM) ($n = 25$ cells, three independent experiments). **d**, Colocalization analysis by TIRFM of endoA2 with the indicated markers. Transient expression in HeLa cells: red fluorescent protein (RFP)-tagged dynamin-2 (DNM2–mRFP), $n = 10$; mRFP-tagged clathrin light chain (mRFP–LCa), $n = 8$; μ2–mCherry, $n = 12$. Genome-edited SK-MEL-2 cells: LCa–mRFP, $n = 8$. Two independent experiments. ***$P < 0.001$ (Bonferroni's multiple comparison test). Scale bars, 2 μm (**a**, **c**, **d**) and 100 nm (**b**). Data are mean ± s.e.m.

[1]Institut Curie — Centre de Recherche, Endocytic Trafficking and Therapeutic Delivery group, 26 rue d'Ulm, 75248 Paris Cedex 05, France. [2]CNRS UMR3666, 75005 Paris, France. [3]U1143 INSERM, 75005 Paris, France. [4]Institut Curie — Centre de Recherche, Membrane and Cell Functions group, CNRS UMR 168, Physico-Chimie Curie, Université Pierre et Marie Curie, 26 rue d'Ulm, 75248 Paris Cedex 05, France. [5]The University of Chicago, Department of Chemistry, 5735 S Ellis Ave, Chicago, Illinois 60637, USA. [6]Institut Curie — Centre de Recherche, Biomimetism of Cell Movement group, CNRS UMR 168, Physico-Chimie Curie, Université Pierre et Marie Curie, 26 rue d'Ulm, 75248 Paris Cedex 05, France. [7]Université Paris Diderot, Sorbonne Paris Cité, 75205 Paris, France. [8]Institute of Structural and Molecular Biology, University College London & Birkbeck College, London WC1E 6BT, UK. [9]Institut Curie — Centre de Recherche, Membrane Dynamics and Mechanics of Intracellular Signaling group, 26 rue d'Ulm, 75248 Paris Cedex 05, France. [10]Vanderbilt School of Medicine, Department of Molecular Physiology and Biophysics, 718 Light Hall, Nashville, Tennessee 37232, USA. [11]CNRS, UMR7592, Institut Jacques Monod, Université Paris Diderot, Sorbonne Paris Cité, 15 rue Hélène Brion, 75205 Paris Cedex 13, France. [12]Medical Research Council, Laboratory of Molecular Biology, Cambridge Biomedical Campus, Francis Crick Avenue, Cambridge CB2 0QH, UK.
*These authors contributed equally to this work.

to the plasma membrane by STxB (Extended Data Fig. 2c and Supplementary Video 2). These results demonstrated that endoA2 localized to sites of STxB and CTxB internalization.

Endophilins have classically been associated with the clathrin pathway (for example, see ref. 12), even if recent studies have indicated that this view may need to be broadened[13,14]. Notably, the overlap of endoA2 with fluorescent-protein-tagged clathrin or the μ2 subunit of the clathrin adaptor AP2 was weak, both in transiently transfected HeLa cells, or genome-edited SK-MEL-2 cells (Fig. 1d and Extended Data Fig. 2d, e). STxB also only weakly colabelled with clathrin pathway markers in both cell systems (Extended Data Fig. 2g–j). By contrast, endoA2 extensively codistributed with dynamin (Fig. 1d and Extended Data Fig. 2f), as expected[5,6].

In endoA2-depleted cells, short and apparently tubular STxB-containing invaginations were observed with sizes at the resolution limit of confocal light microscopy (Extended Data Fig. 3a). Using a nanogold conjugate of STxB that was specifically developed for this study (Extended Data Fig. 3b, c), it could be shown by electron microscopy that these structures were connected to the plasma membrane (Fig. 2a and Extended Data Fig. 3d). Their frequency did not increase after depletion of endoA2 (Fig. 2b, left), whereas their average length significantly increased (Fig. 2b, right). These findings were strongly in favour of a function for endoA2 in scission of STxB-induced endocytic plasma membrane invaginations.

Retrograde STxB trafficking to the *trans*-Golgi network (TGN) in endoA2-depleted cells was quantified using a STxB variant with tandem protein sulfation sites, termed STxB-$Sulf_2$. With different siRNAs that had variable depletion efficiencies (Extended Data Fig. 4a), we found that sulfation of STxB-$Sulf_2$ in TGN membranes was inhibited in a dose-dependent manner with cellular endoA2 levels (Fig. 2c), while STxB cell-surface binding was not decreased (Extended Data Fig. 4b). Depletion of the TGN-localized tSNARE protein syntaxin-16 served as a benchmark treatment[15]. We concluded that endoA2 was required for efficient STxB trafficking into cells. A similar conclusion was reached when CTxB endocytosis was analysed in endoA2-depleted BSC-1 cells (Extended Data Fig. 4c).

In endoA2-depleted cells, the inhibition of STxB transport to Golgi membranes could also be documented by immunofluorescence (Fig. 2d). Expression of siRNA-resistant endoA2 or a SH3 domain deletion mutant (ΔSH3) rescued this phenotype (Fig. 2d and Extended Data Fig. 4d), suggesting that the function of endoA2 in STxB trafficking was independent of SH3 domain interaction with binding partners such as dynamin. By contrast, an amino-terminal amphipathic helix deletion mutant (endoA2ΔH0) failed to rescue STxB trafficking (Fig. 2d and Extended Data Fig. 4d), probably owing to a role of this helix in membrane recruitment (see below). Correspondingly, endoA2ΔSH3 expression reduced STxB-induced tubule length on ATP-depleted cells, similar to wild-type endoA2, whereas endoA2ΔH0 failed to do so (Extended Data Fig. 4e), reinforcing the hypothesis of endoA2 participating in membrane scission.

Depletion of endoA2 did not affect transferrin internalization or recycling, the steady-state localization of the clathrin cargo proteins TGN46 and cation-independent mannose 6-phophate receptor (CI-MPR)[16,17], or anterograde transport of E-cadherin (Extended Data Fig. 5a–c). Clearly, it was the cellular entry of STxB and CTxB that was specifically altered under these conditions. By contrast, depletion of the μ2 chain of AP2 had no effect on STxB trafficking, while transferrin uptake was efficiently blocked (Extended Data Fig. 5d–f).

To address the function of endoA2 in scission, we exploited the knocksideways system[18] to remove endoA2 acutely and reversibly from its normal site of action at the plasma membrane. HeLaM cells were used that expressed (1) the mitochondrial trap construct Mito-YFP-FRB (containing a yeast mitochondrial membrane protein, the yellow fluorescent protein (YFP) reporter and the FKBP-rapamycin-binding (FRB) domain), and (2) endoA2 tagged with both GFP and the rapamycin-binding protein FKBP. In cells with reduced ATP levels, the length of STxB-induced tubules was only slightly increased after depletion of endogenous endoA2 (Fig. 3a and Extended Data Fig. 6a), owing to the presence of the siRNA-resistant FKBP-tagged endoA2 fusion protein. The fusion protein was then sequestered on mitochondria by the addition of rapamycin, after which the length of STxB-containing tubules

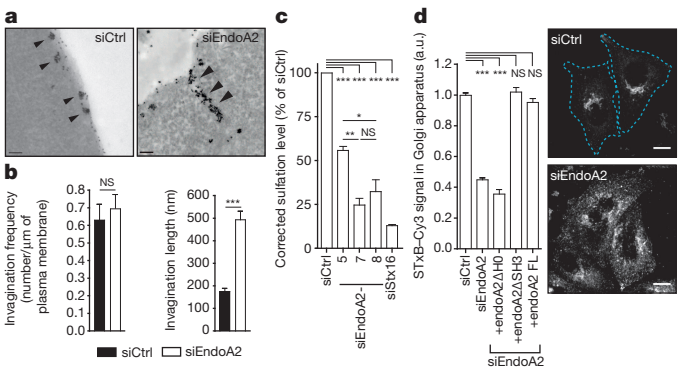


**Figure 2 | EndoA2 functions in Shiga toxin uptake.** **a**, Incubation for 5 min at 37 °C of control siRNA (siCtrl) or endoA2-depleted (siEndoA2) HeLa cells with nanogold-coupled STxB (arrowheads indicate invaginations; representative images of numbers of cells as shown in **b**). **b**, Frequency (siCtrl, $n = 25$ cells; siEndoA2, $n = 27$ cells) and length (siCtrl, $n = 149$ tubules; siEndoA2, $n = 138$ tubules) of STxB-containing invaginations on experiments as in **a**. NS, non significant. $^{***}P < 0.001$ (two-tailed Mann–Whitney $U$ test). **c**, Sulfation analysis ($n = 3$ independent experiments) on HeLa cells, using siRNAs targeting endoA2 (siEndoA2-5, 7 and 8), syntaxin-16 (siStx16) or control siRNA. $^{*}P < 0.05$, $^{**}P < 0.01$, $^{***}P < 0.001$ (Bonferroni's multiple comparison test). **d**, Rescue experiment on endoA2-depleted HeLa cells. Incubation for 45 min at 37 °C with 50 nM STxB–Cy3. One arbitrary unit (a.u.) corresponds to 78.7 ± 1.2% of STxB in Golgi area. Numbers of cells: siCtrl, $n = 145$; siEndoA2, $n = 190$; siEndoA2 plus endoA2ΔH0, $n = 46$; siEndoA2 plus endoA2 lacking the C-terminal SH3 domain (endoA2ΔSH3), $n = 31$; siEndoA2 plus full-length (FL) endoA2, $n = 56$; two independent experiments. $^{***}P < 0.001$ (Bonferroni's multiple comparison test). Scale bars, 100 nm (**a**) and 10 μm (**d**). Data are mean ± s.e.m.

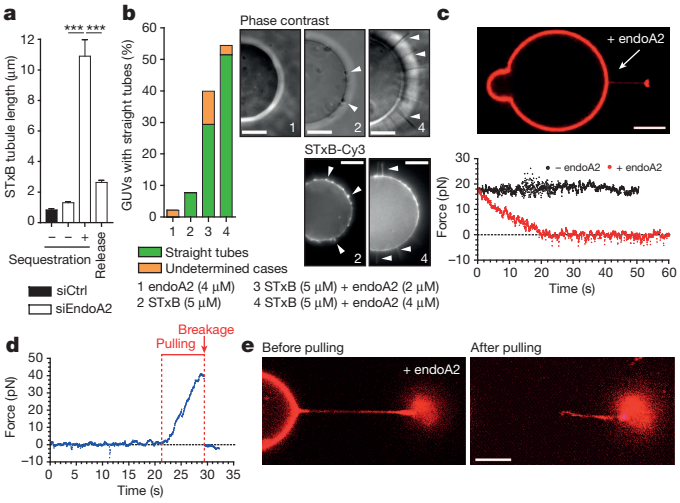


**Figure 3 | Model membrane experiments.** **a**, Knocksideways technique on ATP-depleted HeLaM cells in control (siCtrl) or endoA2-depletion (siEndoA2) conditions. Incubations for 15 min at 37 °C with 0.5 μM STxB. Mean ± s.e.m. of the following numbers of tubules: siCtrl, $n = 65$ (30 cells); without (−) sequestration, $n = 101$ (52 cells); with (+) sequestration, $n = 313$ (131 cells); release, $n = 626$ (187 cells); two independent experiments. $^{***}P < 0.001$ (Dunn's multiple comparison test). **b**, Inverse emulsion technique in conditions 1–4, as indicated. Number of vesicles: 1, $n = 46$; 2, $n = 39$; 3, $n = 17$; 4, $n = 32$; three independent experiments. Arrows point to tubular structures. **c**–**e**, Nanotube tethers. **c**, Tube retraction force in presence (1 μM) or absence of endoA2. Representative of 21 experiments. **d**, **e**, Measurement of retraction force over time upon stepwise elongation at 0.5 μm $s^{-1}$ of an endoA2-scaffolded tube (**d**), and pulling-force-driven scission (**e**). Scale bars, 10 μm (**b**) and 5 μm (**c**, **e**).

significantly increased (Fig. 3a and Extended Data Fig. 6a). This effect was reversible, as rapamycin washout led to significantly shorter tubules (release condition). These results strongly reinforced the idea that endoA2 is involved in the scission of STxB-induced endocytic invaginations.

Controlled model membrane systems were then used to dissect aspects of endoA2 function with respect to membrane tubulation and scission. Cell-sized liposomes that reproduced a key aspect of natural membranes, that is, an asymmetric bilayer composition, were obtained via the inverse emulsion technique[19] (see Methods for leaflet compositions). To permit the acute introduction of endoA2 into the system, its topology was inverted with respect to the cellular situation: when indicated, STxB was included inside liposomes, whereas endoA2 was added to the external medium. Incubation with up to 4 μM endoA2 did not lead to the formation of tubules (Fig. 3b, condition 1). By contrast, liposomes that contained STxB exhibited coiled tubular protrusions (condition 2). Addition of endoA2 to STxB-containing liposomes at concentrations of 2 or 4 μM (Fig. 3b, conditions 3 or 4, respectively) caused tube straightening. Thus, endoA2 prompted the morphological transformation of STxB-induced tubular membranes.

For dynamic measurements, we turned to another setup in which optical tweezers were used to pull membrane tethers mechanically from giant unilamellar vesicles, held with a micropipette[20]. The force exerted by protein binding onto the tether membrane could be directly measured, tube radii controlled in a range from 10 to 100 nm, and tube elongation driven at controlled velocities. After endoA2 injection at concentrations as low as 1 μM (protein concentration inside the injection pipette), the tube retraction force decreased to zero (Fig. 3c), indicating the formation of an external scaffold on the tether membrane, which probably explained the morphological transformation in the asymmetric bilayer system.

We did not observe spontaneous scission of endoA2-scaffolded tubes ($n = 35$). However, when these were pulled further at elongation rates of $\sim$0.5 μm $s^{-1}$, the tube retraction force increased (Fig. 3d), leading to breakage in 15 out of 18 cases (Fig. 3e). Elongation of bare tethers from fluid membranes, at rates as those used in this study, never leads to scission[19,21], and we explicitly confirmed the resilience of bare tubes on forced elongation at an increased rate of $\sim$10 μm $s^{-1}$ ($n = 2$). We speculate that interactions between endoA2 scaffold and the underlying membrane limit the flow of lipids during tube extension, thereby leading to increased membrane tension and spontaneous squeezing of the tube until the scission threshold radius has been reached.

The pulling speed that was required *in vitro* to induce the scission of endoA2-scaffolded tubes was very similar to the speed produced by microtubule-based molecular motors[22], and microtubules have previously been implicated in the cellular entry of Shiga toxin[23]. Interference with microtubule-based functions before reduction of cellular ATP levels led to the loss of micrometre-long STxB-induced tubules (Extended Data Fig. 6b, c), while short (<200 nm) tubules persisted (Extended Data Fig. 7). These findings suggested that STxB-induced invaginations were recognized by molecular motors for the further processing into cells.

As indicated by a change in tube retraction force, the endoA2ΔH0 mutant formed a scaffold only at concentrations above 7 μM (Extended Data Fig. 6d), seven times higher than the minimum concentration required for wild-type endoA2. Furthermore, the radius of the endoA2H0 scaffold was on average twice that of the wild-type endoA2 (23 ± 10 nm, mean ± s.d., $n = 10$, versus 12 ± 4 nm, $n = 6$, respectively). When pulled, endoA2ΔH0-scaffolded tubes nevertheless underwent scission in 5 out of 5 cases (Extended Data Fig. 6e). The N-terminal amphipathic helix thus did not have a decisive role in scission by elongation of scaffolded membrane tubes. Rather, it seemed important for efficient recruitment of endoA2 to the membrane, as well as possibly affecting the molecular organization of the scaffold.

We next investigated the role of endoA2 together with other scission factors that have been shown before to play a part in STxB uptake. The first was actin[10]. EndoA2 and actin strongly and dynamically colocalized (Extended Data Fig. 8a), and even in endoA2-depleted cells actin was localized on STxB-induced membrane invaginations (Extended Data Fig. 8b, c). This indicated that endoA2 was not required for actin recruitment to STxB uptake structures. Interestingly, the depletion of endoA2 or the depolymerization of actin with 0.5 μM latrunculin-A led to a similar increase in the length of STxB-induced tubules, and the concomitant treatment had an additive effect (Fig. 4a and Extended Data Fig. 8d, e). Thus, both endoA2 and actin contributed independently to scission probability in STxB endocytosis. In cells that were depleted of ARPC2 (p34 subunit of the Arp2/3 complex), the length of STxB-induced tubules was similar to that observed in latrunculin-A-treated cells (Fig. 4a and Extended Data Fig. 8f), confirming the specificity of our observations.

After depletion of dynamin, STxB-induced tubules were longer than in control cells[8] (Fig. 4a), and endoA2 was clearly localized on these structures (Extended Data Fig. 9a, bottom). Tubules positive for endogenous endoA2 (Extended Data Fig. 9b) were seen only in the presence of STxB (compare ±STxB panels), in line with our model membrane results. This finding documented that these tubules did not preexist but were indeed induced by STxB. Dynamin was still found in association with STxB uptake structures in endoA2-depleted cells (Extended Data Fig. 9c), indicating that in addition to endoA2, other proteins contribute to dynamin recruitment to membranes[24]. As for actin, concomitant depletion of dynamin and endoA2 had an additive effect on the length of STxB-induced tubules (Fig. 4a and Extended Data Fig. 9d).

Actin, dynamin and endoA2 thus independently contributed to the probability of scission in the STxB uptake pathway. Indeed, when dynamin and endoA2-depleted cells were concomitantly incubated with 0.25 μM latrunculin-A, tubule length increased further, leading to an unprecedented tubulation phenotype throughout the cell population (Fig. 4a and Extended Data Fig. 9d). Importantly, when STxB-induced tubules were binned according to their length (Fig. 4b), a frequency shift was observed when going from unperturbed cells (condition A, red) to cells submitted to single (condition B, yellow), double (condition E, green) or triple (condition H, blue) perturbation. This data representation clearly illustrated that short tubules (most abundant in unperturbed cells) were progressively transformed into long tubules (most abundant in the triple-perturbation condition).

Protein biosynthesis inhibition is an established measure of Shiga toxin arrival in the cytosol[25]. Cells that were depleted of endoA2 or dynamin, or incubated with 0.25 μM latrunculin-A, were only weakly protected against Shiga-like toxin-1 (STx-1; note that STx-1 and Shiga toxin differ by only one residue) (Fig. 4c and Extended Data Fig. 10a–c). These

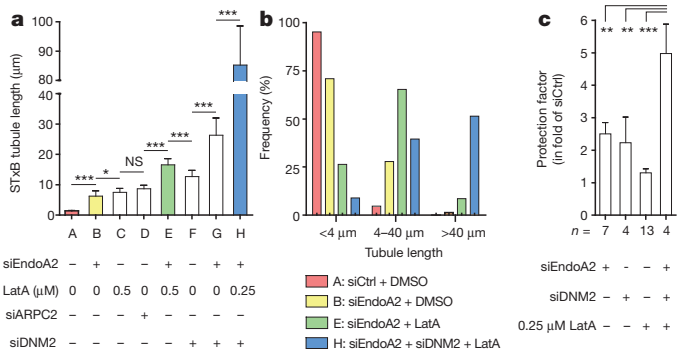


**Figure 4 | Additive effects of scission factors.** **a**, Incubation of HeLa cells for 5 min at 37 °C with 0.5 μM STxB–Cy3. Determination of tube length on fixed cells (number of tubules per condition: A, $n = 254$; B, $n = 79$; C, $n = 94$; D, $n = 146$; E, $n = 118$; F, $n = 338$; G, $n = 131$; H, $n = 115$); two independent experiments. NS, non significant, $*P < 0.05$, $***P < 0.001$ (Dunn's multiple comparison test). LatA, latrunculin-A. **b**, Frequency distribution of tubules according to length (conditions as in **a**). **c**, Intoxication analysis. Protection factors on 4–13 independent experiments per condition. $**P < 0.01$, $***P < 0.001$ (Bonferroni's multiple comparison test). Data are mean ± s.e.m.

individual treatments thus failed to impose a transport block that would shut down access to the cytosol to levels that were required to be robustly detected by this extremely sensitive method. By contrast, triple treatment induced a substantial shift to the right of the intoxication curves (Extended Data Fig. 10d), such that 5.0-fold ($\pm 0.9$, $n = 4$) more STx-1 was required to achieve the same level of protein biosynthesis inhibition as in control conditions (see quantification in Fig. 4c). Clearly, the scission factors endoA2, actin and dynamin needed to be inhibited simultaneously for a substantial protection of cells against STx-1.

Our study reveals a novel function of endoA2 in clathrin-independent endocytosis of Shiga and cholera toxin, and suggests more generally that this BAR domain protein operates preferentially on non-clathrin sites of uptake (see ref. 26). Our data also provide strong evidence for a function of endoA2 in the scission process. In the context of the Shiga toxin model, endoA2 is, to our knowledge, the first cellular factor that was identified to recognize specifically the mechanical signal transmitted by the toxin to the cytosol: a highly curved plasma membrane domain. Unexpectedly, our findings suggest that actin[10] and dynamin[8] contribute in an additive manner with endoA2 to scission in Shiga toxin uptake. They probably act on the same endocytic invaginations and not on parallel uptake events, since the overall length of Shiga-toxin-induced plasma membrane tubules strongly increased in cells in which all three scission factors were inhibited. Such additive function in scission is unexpected and suggests that specificity within given endocytic processes is the result of defined cocktails of modular machinery. This hypothesis does not exclude a functional interaction between scission factors[27,28]. An exciting new modality emerges from our observations that scaffolding by endoA2 sensitizes tether membranes for pulling-force-induced scission. This finding should stimulate further research into the function of cytoskeleton-based molecular motors in scission and the mechanisms by which scaffolding by BAR domain proteins prime membranes to this effect.

**Online Content** Methods, along with any additional Extended Data display items and Source Data, are available in the online version of the paper; references unique to these sections appear only in the online paper.

**Received 15 August; accepted 14 November 2014.**
**Published online 17 December 2014.**

1. Campelo, F. & Malhotra, V. Membrane fission: the biogenesis of transport carriers. *Annu. Rev. Biochem.* **81,** 407–427 (2012).
2. Shnyrova, A. V. *et al.* Geometric catalysis of membrane fission driven by flexible dynamin rings. *Science* **339,** 1433–1436 (2013).
3. Morlot, S. *et al.* Membrane shape at the edge of the dynamin helix sets location and duration of the fission reaction. *Cell* **151,** 619–629 (2012).
4. Faelber, K. *et al.* Crystal structure of nucleotide-free dynamin. *Nature* **477,** 556–560 (2011).
5. Sundborger, A. *et al.* An endophilin-dynamin complex promotes budding of clathrin-coated vesicles during synaptic vesicle recycling. *J. Cell Sci.* **124,** 133–143 (2011).
6. Neumann, S. & Schmid, S. L. Dual role of BAR domain-containing proteins in regulating vesicle release catalyzed by the GTPase, dynamin-2. *J. Biol. Chem.* **288,** 25119–25128 (2013).
7. Howes, M. T., Mayor, S. & Parton, R. G. Molecules, mechanisms, and cellular roles of clathrin-independent endocytosis. *Curr. Opin. Cell Biol.* **22,** 519–527 (2010).
8. Römer, W. *et al.* Shiga toxin induces tubular membrane invaginations for its uptake into cells. *Nature* **450,** 670–675 (2007).
9. Mim, C. & Unger, V. M. Membrane curvature and its generation by BAR proteins. *Trends Biochem. Sci.* **37,** 526–533 (2012).
10. Römer, W. *et al.* Actin dynamics drive membrane reorganization and scission in clathrin-independent endocytosis. *Cell* **140,** 540–553 (2010).
11. Ewers, H. *et al.* GM1 structure determines SV40-induced membrane invagination and infection. *Nature Cell Biol.* **12,** 11–18 (2010).
12. Milosevic, I. *et al.* Recruitment of endophilin to clathrin-coated pit necks is required for efficient vesicle uncoating after fission. *Neuron* **72,** 587–601 (2011).
13. Llobet, A. *et al.* Endophilin drives the fast mode of vesicle retrieval in a ribbon synapse. *J. Neurosci.* **31,** 8512–8519 (2011).
14. Kononenko, N. L. *et al.* Clathrin/AP-2 mediate synaptic vesicle reformation from endosome-like vacuoles but are not essential for membrane retrieval at central synapses. *Neuron* **82,** 981–988 (2014).
15. Amessou, M. *et al.* Syntaxin 16 and syntaxin 5 control retrograde transport of several exogenous and endogenous cargo proteins. *J. Cell Sci.* **120,** 1457–1468 (2007).
16. Draper, R. K., Goda, Y., Brodsky, F. M. & Pfeffer, S. R. Antibodies to clathrin inhibit endocytosis but not recycling to the *trans* Golgi network *in vitro*. *Science* **248,** 1539–1541 (1990).
17. Nesterov, A., Carter, R. E., Sorkina, T., Gill, G. N. & Sorkin, A. Inhibition of the receptor-binding function of clathrin adaptor protein AP-2 by dominant-negative mutant μ2 subunit and its effects on endocytosis. *EMBO J.* **18,** 2489–2499 (1999).
18. Robinson, M. S., Sahlender, D. A. & Foster, S. D. Rapid inactivation of proteins by rapamycin-induced rerouting to mitochondria. *Dev. Cell* **18,** 324–331 (2010).
19. Campillo, C. *et al.* Unexpected membrane dynamics unveiled by membrane nanotube extrusion. *Biophys. J.* **104,** 1248–1256 (2013).
20. Cuvelier, D., Derenyi, I., Bassereau, P. & Nassoy, P. Coalescence of membrane tethers: experiments, theory, and applications. *Biophys. J.* **88,** 2714–2726 (2005).
21. Evans, E. & Yeung, A. Hidden dynamics in rapid changes of bilayer shape. *Chem. Phys. Lipids* **73,** 39–56 (1994).
22. Toba, S., Watanabe, T. M., Yamaguchi-Okimoto, L., Toyoshima, Y. Y. & Higuchi, H. Overlapping hand-over-hand mechanism of single molecular motility of cytoplasmic dynein. *Proc. Natl Acad. Sci. USA* **103,** 5741–5745 (2006).
23. Hehnly, H., Sheff, D. & Stamnes, M. Shiga toxin facilitates its retrograde transport by modifying microtubule dynamics. *Mol. Biol. Cell* **17,** 4379–4389 (2006).
24. Meinecke, M. *et al.* Cooperative recruitment of dynamin and BIN/amphiphysin/Rvs (BAR) domain-containing proteins leads to GTP-dependent membrane scission. *J. Biol. Chem.* **288,** 6651–6661 (2013).
25. Johannes, L. & Römer, W. Shiga toxins - from cell biology to biomedical applications. *Nature Rev. Microbiol.* **8,** 105–116 (2010).
26. Boucrot, E. *et al.* Endophilin marks and controls a clathrin-independent endocytic pathway. *Nature* http://dx.doi.org/10.1038/nature14067 (this issue).
27. Itoh, T. *et al.* Dynamin and the actin cytoskeleton cooperatively regulate plasma membrane invagination by BAR and F-BAR proteins. *Dev. Cell* **9,** 791–804 (2005).
28. Roux, A., Uyhazi, K., Frost, A. & De Camilli, P. GTP-dependent twisting of dynamin implicates constriction and tension in membrane fission. *Nature* **441,** 528–531 (2006).

**Supplementary Information** is available in the online version of the paper.

**Acknowledgements** We would like to acknowledge the following people for help in experiments and providing materials or expertise: A. Berthier, L. Cabanié, K. Carvalho, P. de Camilli, C. Day, D. Drubin, A. El Marjou, V. Fraisier, A. Gautreau, T. Kirchhausen, L. Leconte, C. Merrifield, G. Montagnac, P. Paul-Gilloteaux, M. S. Robinson, L. Sengmanivong and E. Smythe. The facilities as well as scientific and technical assistance from staff in the PICT-IBiSA/Nikon Imaging Centre at Institut Curie-CNRS and the France-BioImaging infrastructure (ANR-10-INSB-04) are acknowledged. This work was supported by grants from the Agence Nationale pour la Recherche (ANR-09-BLAN-283 to L.J. and C.S., ANR-10-LBX-0038 to C.L., ANR-11 BSV2 014 03 to L.J. and P.B., ANR-12-BSV5-0014 to C.S.), the Indo-French Centre for the Promotion of Advanced Science (project no. 3803, L.J.), Marie Curie Actions — Networks for Initial Training (FP7-PEOPLE-2010-ITN, L.J.), European Research Council advanced grant (project 340485, L.J.), Marie Curie International Reintegration Grant (FP7-RG-277078, C.W.), the Royal Society (RG120481, E.B.), Fondation ARC pour la Recherche sur le Cancer (DEQ20120323737, C.S.), National Institutes of Health (RO1 GM106720, A.K.K.), La Ligue contre le Cancer, Comité de Paris (RS08/75-89, A.A.S.), and by fellowships from Fondation ARC pour la Recherche sur le Cancer (H.-F.R., J.L. and M.-D.G.-C.), AXA Research Funds (J.L. and M.-D.G.-C.), the Biological Sciences Research Council (David Phillips Research Fellowship to E.B.), Chateaubriand fellowship and the France and Chicago Collaborating in the Sciences grant (M.S.). The Johannes, Lamaze, Sykes and Bassereau teams are members of Labex CelTisPhyBio (11-LBX-0038) and of Idex Paris Sciences et Lettres (ANR-10-IDEX-0001-02 PSL). P.B.'s group belongs to the French research consortium CellTiss.

**Author Contributions** The following datasets were contributed by the indicated authors: Figs 1b–d, 2–4 and Extended Data Figs 1–3, 4a, b, d, e, 5–10 (H.-F.R.); Fig. 3c–e and Extended Data Fig. 6d, e (M.S.); Fig. 3b (J.L.); Fig. 1a and Extended Data Fig. 4c (E.B.); Fig. 4c and Extended Data Fig. 10 (M.-D.G.-C.); Fig. 2a and Extended Data Fig. 3d (S.A. and V.C.); Fig. 1b and Extended Data Figs 3b, c and 7 (V.C.). C.L., C.W., A.K.K., A.A.S. and H.T.M. provided technical support and conceptual advice. C.S., P.B. and L.J. provided direction and guidance. L.J. conceived the initial design of the study and wrote the first draft. All authors discussed the results and commented on the manuscript.

**Author Information** Reprints and permissions information is available at www.nature.com/reprints. The authors declare no competing financial interests. Readers are welcome to comment on the online version of the paper. Correspondence and requests for materials should be addressed to L.J. (ludger.johannes@curie.fr).

## METHODS

**Antibodies and other reagents.** The following antibodies were purchased from the indicated suppliers: rabbit polyclonal anti-endoA2 for western blotting (Bethyl, A302-349A, 1:2,000) or immunofluorescence and cryo-electron microscopy (Santa Cruz Biotechnology, sc-25495, 1:200 for immunofluorescence and 1:10 for cryo-electron microscopy); rabbit polyclonal anti-STxB (Covalab, 1:100 for cryo-electron microscopy); mouse monoclonal anti-clathrin heavy chain for western blotting (BD Biosciences, 610500, 1:5,000); mouse monoclonal anti-α-tubulin (Sigma, T5168, 1:5,000 for western blotting); rabbit polyclonal anti-syntaxin-16 (Synaptic Systems, 110 163, 1:1,000 for western blotting); rabbit monoclonal anti-giantin (Institut Curie, recombinant proteins platform, A-R-R#05, 1:100 for immunofluorescence); sheep polyclonal anti-TGN46 (Serotec, AHP500G, 1:200 for immunofluorescence); mouse monoclonal anti-CI-MPR (Abcam, ab2733, 1:200 for immunofluorescence); rabbit polyclonal anti-mCherry (Institut Curie, Recombinant proteins platform, A-P-R#13, 1:200 for immunofluorescence); mouse monoclonal anti-GFP (Roche Applied Sciences, 11 814 460 001, 1:1,000 for western blotting); mouse monoclonal anti-dynamin Hudy 1 (Upstate, 05-319, 1:200 for immunofluorescence); mouse monoclonal anti-dynamin (BD Biosciences, 610246, 1:1,000 for western blotting); rabbit polyclonal anti-ARPC2 (Millipore, 07-227, 1:1,000 for western blotting); rabbit polyclonal anti-DYNC1H1 (Proteintech, 12345-1-AP, 1:200 for western blotting); secondary antibodies conjugated to Alexa488, Cy3, Cy5, AMCA or horseradish peroxidase (HRP) (Beckman Coulter and Invitrogen). The mouse monoclonal anti-STxB antibody 13C4 was purified from hybridoma cells (ATCC CRL-1794), and the mouse monoclonal anti-clathrin heavy chain antibody X22 (used at 1:1,000 for immunofluorescence) was a gift from E. Smythe. 2-deoxy-D-glucose, sodium azide, latrunculin-A and nocodazole were purchased from Sigma.

**Cell culture.** HeLa and BSC-1 cells were grown at 37 °C under 5% $CO_2$ in DMEM high glucose glutamax (Invitrogen) supplemented with 10% FCS, 0.01% penicillin-streptomycin and 5 mM pyruvate. Genome-edited SK-MEL-2 cells expressing mRFP–LCa were provided by D. Drubin, and grown at 37 °C under 5% $CO_2$ in DMEM/F12 (Invitrogen) supplemented with 10% FCS, 0.01% penicillin-streptomycin and 5 mM pyruvate. HeLaM cells stably expressing Mito-YFP-FRB were provided by M. S. Robinson. These were grown at 37 °C under 5% $CO_2$ in DMEM high glucose glutamax (Invitrogen) supplemented with 10% FCS, 0.01% penicillin-streptomycin, 5 mM pyruvate and 137.5 μg ml$^{-1}$ hygomycine B. HeLaM Mito-YFP-FRB cells stably expressing C-terminally GFP-FKBP-tagged rat endoA2 were generated for this study (see below) and grown in the same medium as the mother cells, supplemented with 0.5 mg ml$^{-1}$ G418.

**Depletion of cellular ATP.** Cellular ATP was depleted as previously described[8,29]. In brief, cells were incubated for 15–20 min at 37 °C in PBS$^{++}$ supplemented with 10 mM 2-deoxy-D-glucose and 10 mM $NaN_3$.

**DNA constructs and transfection.** Expression plasmids for C-terminally GFP-tagged rat endoA2 (P. De Camilli), mCherry-tagged μ2 subunit of AP2 (C. Merrifield), mRFP-tagged dynamin-2 or clathrin light chain (LCa) (T. Kirchhausen) were provided by the indicated colleagues.

A bicistronic vector encoding SBP-mCherry-E-cadherin and KDEL-streptavidin, used for the anterograde E-cadherin transport assay, was provided by F. Perez, and a plasmid encoding LifeAct-mCherry[30,31] by P. Chavrier.

GFP-tagged mutants of endoA2 (ΔH0 lacking N-terminal amphipatic H0 helix, and ΔSH3 lacking C-terminal SH3 domain) were obtained by PCR from full-length endoA2.

For knocksideways with endoA2, a C-terminally GFP-FKBP-tagged rat endoA2 construct was engineered. For this, rat endoA2–GFP and the FKBP sequence bearing a stop codon were amplified by PCR from plasmids (for amplification of endoA2-GFP fragment, forward primer was 5′-ATACTTAAGATGTCGGTGGCGGGGGCTGAAG-3′ and reverse primer was 5′-TTCCACCTGCACTCCCATCCCTCCGCCCTTGTACAGCTCGTCCAT-3′; for amplification of FKBP fragment, forward primer was 5′-ATGGACGAGCTGTACAAGGGCGGAGGGATGGGAGTGCAGGTGGAA-3′ and reverse primer was 5′-AGTGCGGCCGCTTATTCCAGTTTTAGAAGCTC-3′). The PCR fragments were designed in such a way that they possessed overlapping sequences. This allowed obtaining an endoA2–GFP–FKBP fragment via a third PCR on the two previous fragments with appropriate primers (forward primer from endoA2-GFP amplification: 5′-ATACTTAAGATGTCGGTGGCGGGGCTGAAG-3′; reverse primer from FKBP fragment amplification: 5′-AGTGCGGCCGCTTATTCCAGTTTTAGAAGCTC-3′). After insertion in a pIRESneo2 vector between AflII and NotI restriction sites, clones were validated by sequencing.

For immunofluorescence and live-cell imaging experiments, plasmids were transfected with FuGene 6 (Promega) according to the manufacturer's instructions, or using the classical calcium phosphate procedure[32]. Cells were used for experiments 16–24 h after transfection. For the production of a HeLaM Mito-YFP-FRB cell line stably expressing endoA2–GFP–FKBP, the pIRESneo2/endoA2–GFP–FKBP plasmid was transfected by electroporation, and clones were selected with 0.5 mg ml$^{-1}$ G418.

**RNA interference.** Most siRNAs used in this study were purchased from Qiagen and transfected with HiPerFect (Qiagen) according to manufacturer's instructions. Experiments were performed 72 h after siRNA transfection, where protein depletion efficiency was maximal as shown by immunoblotting analysis with specific antibodies (routinely 80–90%). For most experiments, cells were replated 24 h before use, according to the need of the experiment. AllStars Negative Control siRNA served as a reference point. The depletion of endoA2 was achieved with three different sequences at final concentrations between 2 and 10 nM: 5 (SI03057250: 5′-CACCAGCAAGGCGGTGACAGA-3′), 7 (SI03073931: 5′-CATGCTCAACACGGTGTCCAA-3′) and 8 (SI03108049: 5′-TACACTAGCGCTGACTCCCAA-3′). For syntaxin-16 depletion, a custom-made siRNA sequence was used[15] at concentrations between 2 and 10 nM (5′-AAGCAGCGATTGGTGTGACAA-3′); for dynamin-2, a single siRNA at 10 nM (SI02654687: 5′-CTGCAGCTCATCTTCTCAAAA-3′); for α-adaptin, a single siRNA sequence[33] at concentrations between 10 and 40 nM (5′-AAATGGCGGTGGTGTCGGCTC-3′, Dharmacon); for ARPC2, a smartpool of 4 siRNA sequences (L-012081-00, Dharmacon: 5′-CCATGTATGTTGAGTCTAA-3′, 5′-GCTCTAAGGCCTATATTCA-3′, 5′-GGACAGAGTCACAGTAGTC-3′ and 5′-GTACGGGAGTTTCTTGGTA-3′) at 40 nM.

For endoA2 depletion from BSC-1 cells, a single all Stealth siRNA was used (HSS109705, Invitrogen: 5′-GCTGACCAACCAGATCGATGAGAAC-3′). Cells seeded on 12 mm coverslips placed in 24-well plates (for microscopy) or on glass-bottom 96-well plates (plate-reader experiments) were transfected twice (on days 1 and 2) with oligofectamine (Life Technologies) complexed to 8 or 1.6 pmol, respectively, of HSS109705 siRNA and analysed on day 4 (72 h after the first transfection).

**Recombinant proteins.** Recombinant wild-type STxB, STxB-Cys and STxB-Sulf$_2$ were purified from bacterial periplasmic extracts as previously described[34]. C-terminally Strep-tagged mouse endoA2 and endoA2ΔH0 (N-terminal amphipatic helix deletion mutant) were expressed in bacteria and purified on a Strep-Tactin column (IBA), as previously described[35]. See Supplementary Information for more details.

**Light microscopy.** For immunofluorescence studies, cells were maintained at 37 °C during the full duration of the experiment and during fixation (4% paraformaldehyde) to preserve the integrity of STxB-induced tubules. After quenching with 50 mM $NH_4Cl$ and permeabilization with saponin (0.5% saponin, 2% BSA in PBS), cells were incubated with primary and secondary antibodies, and mounted with Mowiol.

Fixed samples were imaged with a Nikon A1R confocal microscope equipped with a CFI Plan Apo VC 60× numerical aperture (NA) 1.4 oil immersion objective, when not specified otherwise. Wide field images were acquired on a Leica DM 6000B epifluorescence inverted microscope equipped with a HCX PL Apo 63× NA 1.40 oil immersion objective and an EMCCD camera (Photometrics CoolSNAP HQ). Super resolution images were acquired on a N-SIM (Structured Illumination Microscopy, Nikon) equipped with a CFI Apo TIRF 100× NA 1.49 oil immersion objective and an EMCCD camera (Photometrics CoolSNAP HQ2).

For live-cell imaging, cells were grown to subconfluence on FluoroDish chambers with integrated glass coverslips (World Precision Instruments). All observations were made at 37 °C and 5% $CO_2$. Different imaging devices were used. Plasma membrane images were acquired on a TIRF video microscope (Nikon) equipped with a CFI Apo TIRF 100× NA 1.49 oil objective and an EMCCD camera (Photometrics HQ2). Other live-cell images were acquired on spinning disk confocal devices (Nikon) equipped with EMCCD cameras (Photometrics CoolSNAP HQ2). Montages, kymographs and videos were prepared with ImageJ or Fiji (NIH) and MetaMorph Software.

**BAR domain screening.** After 24 h transfection of HeLa cells with fluorescent-protein-tagged constructs, cells were ATP-depleted for 20 min, incubated for 20 min with 1 μM STxB–Cy3 or STxB-Alexa488, fixed at 37 °C, mounted, and viewed by confocal microscopy. The initial phenotype that was scored was BAR domain protein localization on STxB-induced plasma membrane invaginations.

**Electron microscopy.** Two different cell embedding techniques were used: cryoprotection and epon. For further details, see Supplementary Information.

**STxB sulfation.** The sulfation assay was performed as previously described[36]. For further details, see Supplementary Information.

**CTxB internalization.** Alexa555-labelled CTxB (Life Technologies) was used at 0.9–5 nM (50–285 ng ml$^{-1}$) and incubated on cells directly at 37 °C and 5% $CO_2$ (without pre-incubation on ice) for up to 10 min. After incubation, samples destined for microscopy were quickly washed once and fixed at 37 °C with pre-warmed 3.7% paraformaldehyde (PFA) in PBS (20 min, 37 °C). Samples were then washed (twice with PBS and once with 50 mM $NH_4Cl$ in PBS), immunostained and imaged on a laser-scanning confocal microscope (TCS Sp5 AOBS; Leica). For CTxB uptake assay, cells grown in 96-well glass bottom black plates (Thermo Scientific) were incubated with 5 nM toxin for 10 min at 37 °C, moved on ice to stop further endocytosis, washed once with ice-cold PBS to remove unbound toxin and twice with an ice-cold low pH solution (300 mM NaCl, 5 mM KCl, 1 mM $CaCl_2$, 1 mM $MgCl_2$, 0.2 M acetic acid, pH 2.5, as described previously[37,38]), which removed 90 ± 6% of

the cell surface signals ($n = 3$, $P < 0.0001$, two tailed $t$-test) as compared to samples incubated with the toxin on ice (surface staining). The samples were then further washed twice with ice-cold PBS (to increase the pH back to 7.4) and finally fixed on ice with 3.7% PFA for 30 min. Cells were then washed twice with PBS and once with 50 mM $NH_4Cl$ in PBS and incubated with 4′,6-diamidino-2-phenylindole (DAPI) to label their DNA (used to normalize the number of cells in between samples and experiments). Signals from internalized CTxB-Alexa555 (protected from the acid wash) and DAPI were measured using a plate reader (FLUOstar Optima, BMG).

**Intoxication.** The intoxication assay with STx-1 holotoxin was performed as previously described[39]. For further details, see Supplementary Information.

**Knocksideways.** The knocksideways technique was adapted to endoA2, as described[40]. For further details, see Supplementary Information.

**Flow cytometry.** siRNA transfected or PPMP-treated cells (as control) were detached using 4 mM EDTA and incubated for 30 min on ice with transferrin-Alexa647 (Tf-A647; 10 μg ml$^{-1}$) and STxB-cysteine-Alexa488 (1 μM) in PBS$^{++}$ containing 0.2% BSA. After washing in ice-cold PBS, fluorescence was measured with a LSR-II flow cytometer (BD Biosciences). Single-stained samples were used to verify that the fluorescence from each fluorophore was only detected in the expected channel.

**Transferrin endocytosis.** The endocytosis assay was performed essentially as previously described[36]. For further details, see Supplementary Information.

**Transferrin recycling.** Cells were incubated for 40 min at 37 °C with biotinylated transferrin with a disulfide bond (Tf-SS-biot; 60 μg ml$^{-1}$) in PBS$^{++}$ supplemented with 5 mM glucose and 0.2% BSA. After washing, cells were aliquoted (150,000 cells per data point) and placed for the indicated times at 37 °C in PBS$^{++}$ supplemented with 5 mM glucose and 0.2% BSA in the presence of a 50-fold molar excess of non-biotinylated holo-Tf (Sigma-Aldrich). The cells were placed on ice, washed in PBS$^{++}$, and lysed in 10 mM Tris-HCl, pH 7.4, 50 mM NaCl, 1 mM EDTA, 0.2% BSA, 0.1% SDS, 1% Triton X-100. The amount of cell-associated biotinylated transferrin was determined by ELISA, as in the endocytosis assay.

**Anterograde E-cadherin transport.** The retention using selective hooks (RUSH) system was used to quantify anterograde transport of E-cadherin, as previously described[41]. For further details, see Supplementary Information.

**Asymmetric liposomes produced by inverted emulsion.** Lipids and reagents. Egg phosphatidylcholine (EPC), cholesterol, L-α-phosphatidylinositol-4,5-bisphosphate (PtdIns(4,5)$P_2$) and brain total lipid extract were purchased from Avanti Polar Lipids. Ceramide trihexosides (Gb3) was purchased from Matreya LLC. All chemicals, including mineral oil were purchased from Sigma Aldrich unless specified otherwise.

Buffer composition. Inside buffer: 25 mM HEPES, pH 7.4, 100 mM NaCl, 0.5 mM EGTA and 75 mM sucrose. Outside buffer: 25 mM HEPES, pH 7.4, 100 mM NaCl, 0.5 mM EGTA, 0.05 mg ml$^{-1}$ β-casein and 75 mM glucose.

Liposome preparation. Asymmetric liposomes were obtained using an inverted emulsion technique[42,43]. Lipids were dissolved in mineral oil at a total concentration of 0.5 mg ml$^{-1}$, with a composition of egg phosphatidylcholine:cholesterol:Gb3 at a molar ratio of 65:30:5 (inner leaflet) or of brain total lipid extract: PtdIns(4,5)$P_2$ at a mass ratio of 95:5 (outer leaflet). A volume of 2.5 ml of each oil–lipid mixture was sonicated in a bath at 35 °C for 30 min at a power of 30 W, cooled and stored for 1 day at room temperature. A volume of 30 μl of the outer leaflet oil–lipid mixture was poured in a tube on top of the same volume of the outside buffer. The tube was left at room temperature for at least 2 h. In the meantime, an emulsion was obtained by mixing a volume of 250 μl of inner leaflet oil–lipid mixture with 1.25 μl of inside buffer (with or without proteins) and by pumping back-and-forth with a syringe. Then, 50 μl of this emulsion was slowly added to the top phase of the tube and immediately centrifuged at 250*g* for 5 min. Asymmetric liposomes were thus obtained at the bottom of the tube and were collected by removing the upper oil phase.

Liposome observation. Liposomes were observed with an IX70 Olympus inverted microscope equipped with a Olympus 100 oil-immersion phase-contrast objective, numerical aperture (NA) 1.35 (Olympus). Fluorescent Shiga toxin was excited by a 200 W mercury lamp (OSRAM). Images were acquired with a cooled CCD camera CoolSNAP ES (Photometrics).

**Preparation of giant unilamellar vesicles.** Brain total lipid extract, 1,2-distearoyl-*sn*-glycero-3-phosphoethanolamine-*N*-[biotinyl(polyethyleneglycol)-2000] (DSPE-PEG(2000)-biotin), and PtdIns(4,5)$P_2$ were purchased from Avanti Polar Lipids. BODIPY-TR-C5-ceramide was obtained from Molecular Probes. All reagents used to make buffers and β-casein from bovine milk (>99%) were purchased from Sigma-Aldrich.

Giant unilamellar vesicles (GUVs) were prepared by electroformation on platinum wires. Approximately 5 μl of the lipid mix, containing ~95% brain total extract, 5% PtdIns(4,5)$P_2$, ~0.3% DSPE-PEG(2000)-biotin and 0.5% BODIPY-TR-C5-ceramide (all molar fractions), was deposited on platinum wires at 3 g l$^{-1}$, and dried under vacuum for 1 h. GUVs were grown overnight in a mixture of 200 mM sucrose, 50 mM NaCl, 20 mM HEPES, pH 7.4, at $\nu = 500$ Hz, $I = 0.25$ V, $t = 4$ °C.

**Tether-pulling experiments and data analysis.** An experimental chamber, consisting of two parallel coverslips, spaced a few millimetres from each another, was immersed in a 5 g l$^{-1}$ solution of β-casein for 30 min to passivate the glass surface. The chamber was filled with 5–10 μl of the electroformation solution and 200 μl buffer solution (200 mM glucose, 50 mM NaCl, 20 mM HEPES, pH 7.4). The chamber was sealed with oil after ~10 min to prevent evaporation. GUVs with visible fluctuations were aspirated in a micropipette. Membrane tension was controlled via the aspiration pressure. A tether was created by bringing in contact the GUV with a streptavidin-coated polystyrene bead, approximately 3 μm in diameter (Spherotec), trapped with optical tweezers. Using another micropipette, endoA2 was injected in the vicinity of the GUV (at bulk concentrations in the micropipette 0.3–5 μM per monomer for the wild type and 5–7 μM for the endoA2ΔH0 mutant). The force measurements were then repeated.

Pulling-force induced fission. After a scaffold has formed, confirmed with the drop in force, the source of the protein was removed and the tether was further elongated at a rate of 0.5 μm s$^{-1}$.

The radius of the tube was determined from the intensity of the fluorescence signal of the tube, considering that the ratio of fluorescence intensities of lipids inside the tube and inside the vesicle is proportional to the surface of the tube. To get absolute values, we used a normalization factor determined previously[44].

**Image quantifications.** All image quantifications were performed with ImageJ or Fiji (NIH) and Matlab (MathWorks).

**Quantification of STxB transport to the Golgi apparatus.** *Z*-stacks were acquired on images of cells in defined experimental conditions. STxB–Cy3 fluorescence intensities were measured with ImageJ software (NIH) on *z*-projections, either from the entire cell, or from the Golgi region, as defined by giantin labelling. The ratio was then calculated as an index of Golgi localization.

**Quantification of transferrin-Alexa488 endocytosis.** The mean intensity of transferrin-Alexa488 fluorescence in the cell area was measured with ImageJ software (NIH) as above on *z*-projections, after background correction. Mean fluorescence intensities of control conditions were considered as 100%.

**Quantification of colocalization on TIRF images.** To quantify the colocalization between two channels, an object-based method was used, as implemented in JACoP[45], based on the coincidence between two centroids with a 0.5 pixel tolerance. This was achieved in an ImageJ macro by first segmenting the tagged proteins by spot detection in each channel, finding their position, and growing them by dilation to 0.5 pixel radius. The spot detection consisted in finding maxima on the smoothed image (3 × 3 average filter) using the 'find maxima' plugin of ImageJ, whose noise tolerance parameter was set up visually independently for each channel. The results were expressed as the percentage of colocalized spots over the total number of spots in the red and the green channel, respectively.

**Quantification of endoA2–GFP recruitment to the plasma membrane.** Spinning disk time series at fixed *z*-positions were acquired for 80 s at 37 °C with 0.84 s intervals and an exposure time of 80 ms for each channel. STxB was added 15 s after the beginning of each time series. Images were then treated with Fiji. Plasma membrane segments were selected randomly and linear regions of interest (ROI) were drawn. The mean fluorescence along ROI was measured in each channel over all images of a time series. Data were plotted for fluorescence intensity (in percentage of maximum intensity) over time (in seconds).

**Quantification of endoA2 spot lifetime.** Kymographs were obtained from image stacks using MetaMorph Software. Kymographs were processed using a first Fiji macro. The first step consisted in the creation of background images that were subtracted from the original images. Background images were obtained using the 'remove outliers' plugin with a 5-pixel radius and a 50 grey level threshold. An automatic threshold was then proposed and adjusted visually to select the tracks. Selected tracks were saved in ROI files for each image. A second macro was then used to measure the length of tracks, with a step allowing manual correction of ROI, if required. The lifetime of each structure was extracted from the length of the bounding boxes of the segmented tracks in the kymographs, corresponding to their length in frames.

**Quantification of STxB-induced tubule length.** The quantification of STxB-induced tubule length was achieved in batch for all images by segmenting the tubular structures and skeletonizing them so that the number of pixels of tubules was proportional to their length. For this, we used a Fiji macro based on the enhancement of tubular structures by computing eigenvalues of the hessian matrix on a Gaussian filtered version of the image (sigma = 1 pixel), as implemented in the tubeness plugin. The tubules were then thresholded and structures containing less than 3 pixels were discarded. A visual check was performed and a manual correction of segmented tubules was done, if required. The segmented and corrected structures were then reduced to a 1-pixel thick skeleton, using the Fiji plugin 'skeletonize'. Data were grouped by conditions and the length of skeletonized tubules in pixels was converted in micrometer units using Matlab (MathWorks).

**Statistical analyses.** All statistical analyses were performed using Prism v4.0 software (Graphpad Inc). Data were tested for Gaussian distribution with Kolmogorov–Smirnov test (with Dallal–Wilkinson–Lillie for *P* value). In case of non-Gaussian distribution, the following non-parametric tests were used: two-tailed Mann–Whitney *U* test if there were only two conditions or one-way ANOVA (Kruskal–Wallis test) with a Dunn's test if there were more than two data groups to compare. In case of Gaussian distribution, the following parametric tests were used: two-tailed *t*-test for the comparison of the means if there were only two conditions to compare, parametric one-way ANOVA with a Bonferroni test if there were more than two data groups. Significance of mean comparison is represented on the graphs by asterisks. All error bars denote s.e.m., except if stated otherwise. No statistical method was used to predetermine sample size.


29. Zha, X. *et al.* Sphingomyelinase treatment induces ATP-independent endocytosis. *J. Cell Biol.* **140,** 39–47 (1998).
30. Lizárraga, F. *et al.* Diaphanous-related formins are required for invadopodia formation and invasion of breast tumor cells. *Cancer Res.* **69,** 2792–2800 (2009).
31. Riedl, J. *et al.* Lifeact: a versatile marker to visualize F-actin. *Nature Methods* **5,** 605–607 (2008).
32. Jordan, M., Schallhorn, A. & Wurm, F. M. Transfecting mammalian cells: optimization of critical parameters affecting calcium-phosphate precipitate formation. *Nucleic Acids Res.* **24,** 596–601 (1996).
33. Montagnac, G. *et al.* Decoupling of activation and effector binding underlies ARF6 priming of fast endocytic recycling. *Curr. Biol.* **21,** 574–579 (2011).
34. Mallard, F. & Johannes, L. in *Shiga Toxin Methods and Protocols* Vol. 73 (eds Philpott, D. & Ebel, F.) Ch. 17, 209–220 (Humana Press, 2003).
35. Gortat, A., San-Roman, M. J., Vannier, C. & Schmidt, A. A. Single point mutation in Bin/Amphiphysin/Rvs (BAR) sequence of endophilin impairs dimerization, membrane shaping, and Src homology 3 domain-mediated partnership. *J. Biol. Chem.* **287,** 4232–4247 (2012).
36. Amessou, M., Popoff, V., Yelamos, B., Saint-Pol, A. & Johannes, L. Measuring retrograde transport to the *trans*-Golgi network. *Curr. Protoc. Cell. Biol.* **Chapter 15,** Unit–15.10 (2006).
37. Singh, R. D. *et al.* Selective caveolin-1-dependent endocytosis of glycosphingolipids. *Mol. Biol. Cell* **14,** 3254–3265 (2003).
38. Wolf, A. A. *et al.* Ganglioside structure dictates signal transduction by cholera toxin and association with caveolae-like membrane domains in polarized epithelia. *J. Cell Biol.* **141,** 917–927 (1998).
39. Stechmann, B. *et al.* Inhibition of retrograde transport protects mice from lethal ricin challenges. *Cell* **141,** 231–242 (2010).
40. Robinson, M. S. & Hirst, J. Rapid inactivation of proteins by knocksideways. *Curr. Protoc. Cell Biol.* **61,** 15.20.1–15.20.7 (2013).
41. Boncompain, G. & Perez, F. Synchronizing protein transport in the secretory pathway. *Curr. Protoc. Cell Biol.* **Chapter 15,** Unit–15.19 (2012).
42. Pautot, S., Frisken, B. J. & Weitz, D. A. Engineering asymmetric vesicles. *Proc. Natl Acad. Sci. USA* **100,** 10718–10721 (2003).
43. Pontani, L. L. *et al.* Reconstitution of an actin cortex inside a liposome. *Biophys. J.* **96,** 192–198 (2009).
44. Sorre, B. *et al.* Nature of curvature coupling of amphiphysin with membranes depends on its bound density. *Proc. Natl Acad. Sci. USA* **109,** 173–178 (2012).
45. Bolte, S. & Cordelieres, F. P. A guided tour into subcellular colocalization analysis in light microscopy. *J. Microsc.* **224,** 213–232 (2006).

**a**

| Gene name | Other name | Subfamily | Species |
|---|---|---|---|
| ACAP1 | Centaurin β1 | BAR-PH | Human |
| AMPH | Amphiphysin-1 | N-BAR | Human |
| SH3GL1 | Endophilin-A2 | N-BAR | Rat |
| SNX9 | Sortin Nexin 9 | PX-BAR | Mouse |
| APPL1 | | BAR-PH | Mouse |
| CIP4 | Toca-2 | F-BAR | Mouse |
| FBP17 | Toca-3 | F-BAR | Human |
| FCHo1 | | F-BAR | Mouse |
| FCHo2 | | F-BAR | Mouse |
| PACSIN2 | Syndapin-2 | F-BAR | Mouse |
| FNBP1L | Toca-1 | F-BAR | Human |
| BIN1 (AMPHL) | Amphiphysin-2 | N-BAR | Human |
| DNMBP isoform 1 | Full length Tuba | BAR | Mouse |
| DNMBP isoform 2 | Mini-Tuba | BAR | Mouse |
| PICK1 | | BAR | Rat |
| GRAF1 | | BAR-PH | Human |
| SH3GLB1 | Endophilin-B1 | N-BAR | Human |

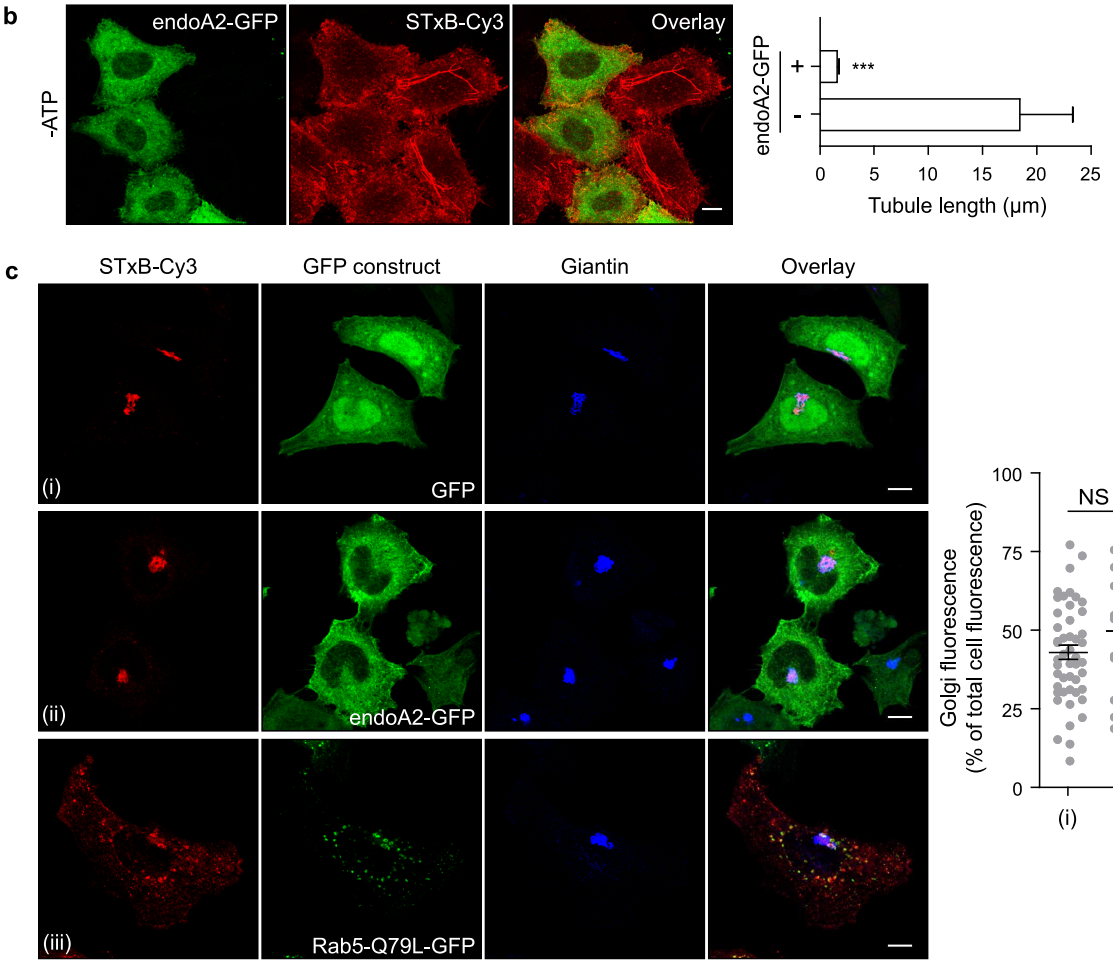


**Extended Data Figure 1 | Screening of BAR domain protein library.** **a**, Listing of BAR domain proteins that were tested in our localization screen. Toca-1, Toca-3 and amphiphysin-2 (yellow underlay) colocalized with STxB on tubular structures (not shown). See below for endoA2 (green underlay). **b**, At variance with the expected phenotype, expression of GFP-tagged endoA2 (green) led to the disappearance of long STxB-induced plasma membrane invaginations (red). Tubule length was quantified in non-transfected control cells ($n = 50$) and endoA2–GFP-expressing cells ($n = 59$). Quantifications show mean ± s.e.m. of two independent experiments. $^{***}P < 0.001$ (two-tailed Mann–Whitney $U$ test). **c**, STxB–Cy3 (50 nM, red) was incubated for 45 min at 37 °C with cells expressing GFP (i), endoA2–GFP (ii) or Rab5(Q79L)–GFP (iii). Expression of endoA2–GFP did not affect STxB trafficking to the Golgi/TGN membranes. $n = 48$ for GFP-expressing cells, $n = 43$ for endoA2–GFP-expressing cells, and $n = 46$ for Rab5(Q79L)–GFP expressing cells; two independent experiments. Quantifications show mean ± s.e.m. NS, non significant; $^{***}P < 0.001$ (Bonferroni's multiple comparison test). Scale bars, 10 μm.

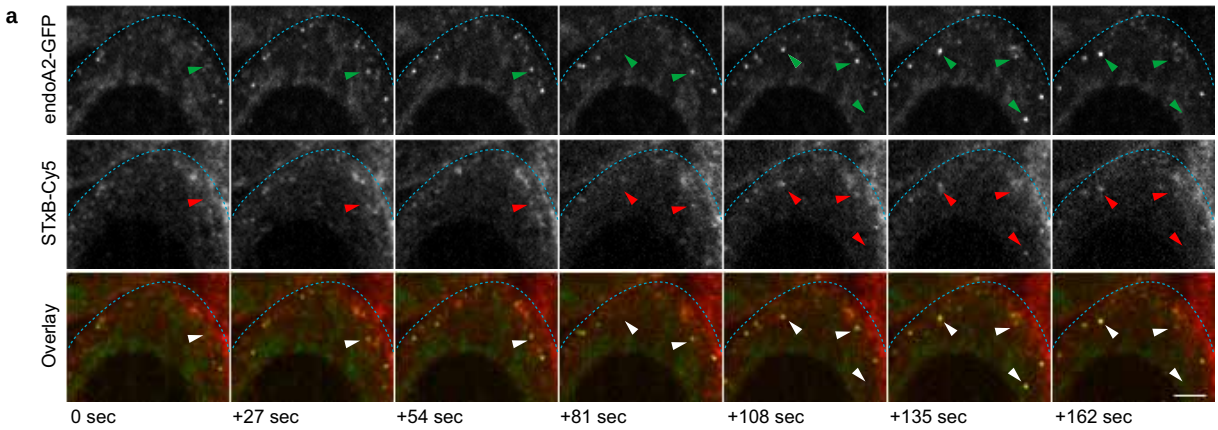


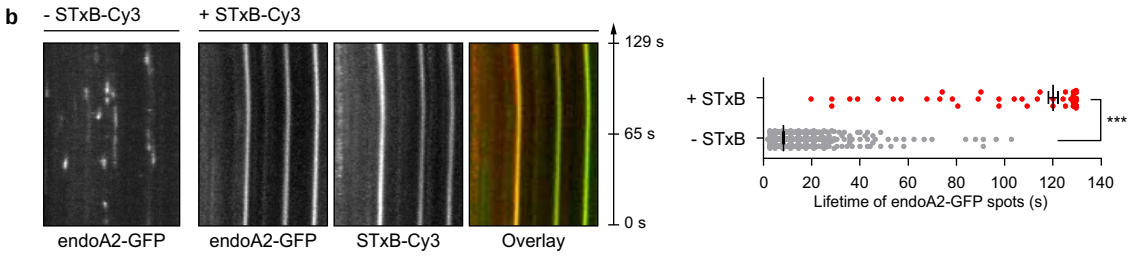


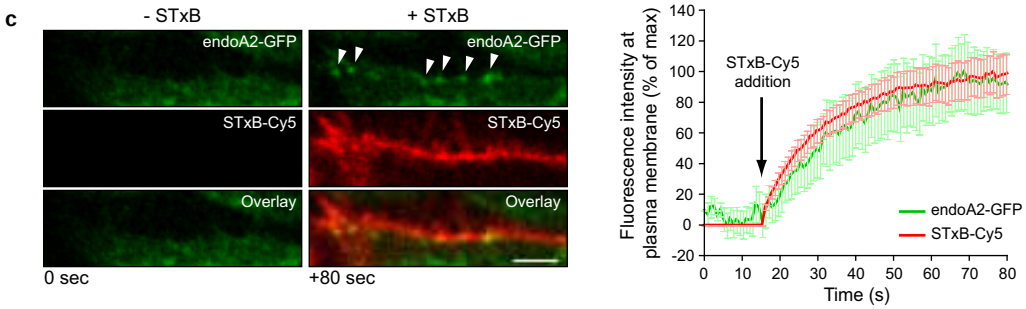


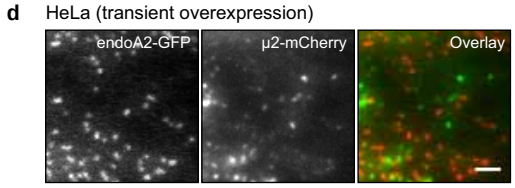


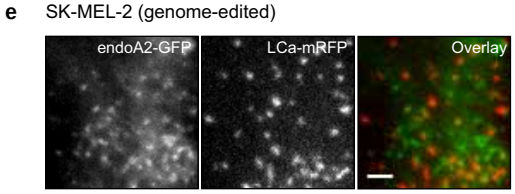


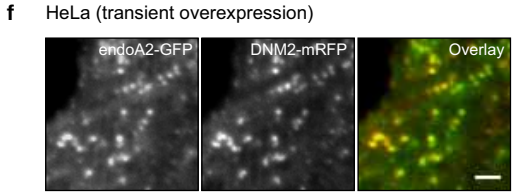


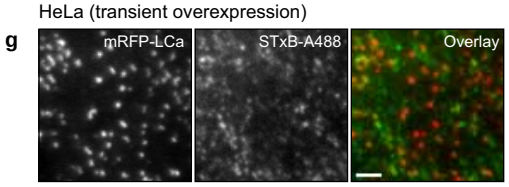


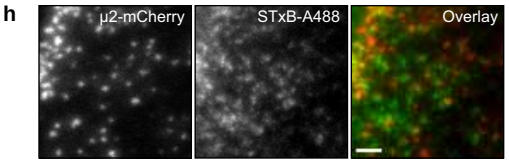


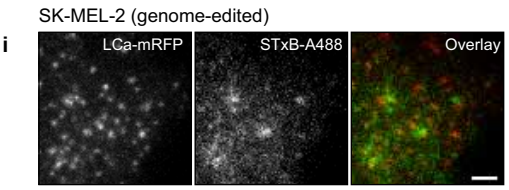


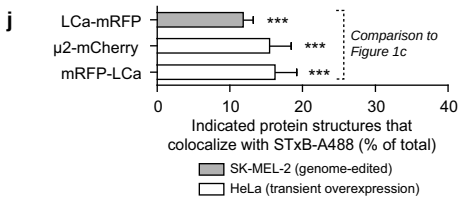

**Extended Data Figure 2 | Intracellular localization analysis of endoA2 and STxB.** **a**–**c**, STxB is internalized in endoA2–GFP-positive vesicles and induces the recruitment of endoA2–GFP to the plasma membrane. HeLaM cells stably expressing endoA2–GFP–FKBP (**a**, **c**), or HeLa cells transiently expressing endoA2–GFP (**b**) were incubated continuously at 37 °C respectively with 0.2 μM STxB–Cy5 or 0.5 μM STxB–Cy3. Observation by live-cell imaging using a spinning disk microscope (**a**, **c**) or TIRFM (**b**). **a**, STxB endocytosis. Image series of 170 s (for the complete sequence, see Supplementary Video 1). Arrows show the formation in the cell periphery of STxB–Cy5 and endoA2–GFP-positive vesicles that move into cells. **b**, Kymographs of HeLa cells transiently expressing endoA2–GFP in the absence (−) or presence (+) of STxB–Cy3. Quantification from TIRFM recordings of endoA2–GFP spot lifetime (−STxB, $n = 1{,}768$ events; +STxB, $n = 144$ events; three independent experiments. $^{***}P < 0.001$ (two-tailed Mann–Whitney $U$ test). **c**, Plasma membrane recruitment of endoA2. STxB–Cy5 was added 15 s after the beginning of image acquisition. Two time points are shown (for the complete sequence, see Supplementary Video 2): before STxB addition (−STxB, 0 s) and after STxB addition (+STxB, +80 s). A striking recruitment of endoA2–GFP to the plasma membrane was observed (white arrowheads). Fluorescence intensities along plasma membrane segments of endoA2–GFP and STxB–Cy5 were followed over time (means ± s.e.m., $n = 6$ cells, three independent experiments). Note that both rose in a similar manner. **d**–**i**, EndoA2 and Shiga toxin poorly colocalize with markers of clathrin-mediated endocytosis. All images show live-cell TIRFM recordings. **d**, HeLa cells were transfected with plasmids expressing endoA2–GFP and μ2–mCherry. The overlap between both markers was very small. **e**, The genome-edited cell line SK-MEL-2 expressing LCa–mRFP was transfected transiently with the endoA2–GFP plasmid. Again, both markers showed very little overlap. **f**, HeLa cells were transfected with plasmids expressing endoA2–GFP and DNM2–mRFP. A substantial overlap was observed between both markers. For **d**–**f**, quantifications are reported in Fig. 1d. **g**–**i**, HeLa cells transiently expressing mRFP–LCa (**g**) or μ2–mCherry (**h**), and the genome-edited cell line SK-MEL-2 expressing LCa–mRFP (**i**) were continuously incubated with 0.5 μM STxB-Alexa488 for 5 min at 37 °C. Note the weak overlap between STxB and the other markers. **j**, Quantification of colocalization for **g**–**i**. Mean ± s.e.m. of the following numbers of cells: mRFP–LCa, $n = 11$; μ2–mCherry, $n = 6$; LCa–mRFP, $n = 19$; two independent experiments. $^{***}P < 0.001$ (Bonferroni's multiple comparison test). Scale bars, 2 μm.

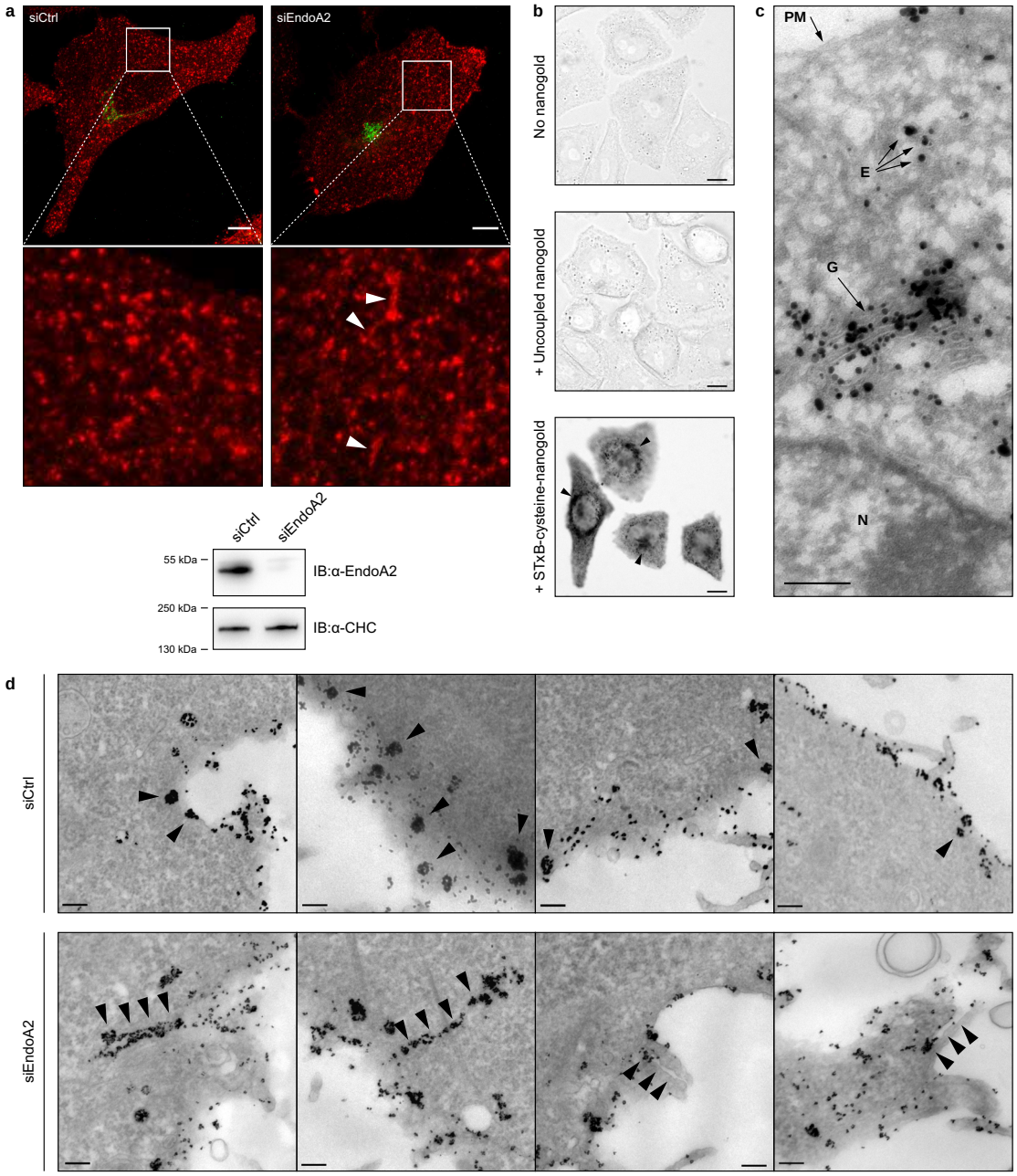


**Extended Data Figure 3 | Effect of endoA2 depletion on Shiga toxin endocytosis at early times of uptake.** **a**, After binding on ice for 30 min, STxB–Cy3 (50 nM, red) was incubated for 5 min at 37 °C with HeLa cells that had been transfected with negative control siRNAs (18 images), or siRNAs against endoA2 (23 images). After fixation, Golgi membranes were labelled with antibodies against giantin (green). Note the presence of short STxB-containing tubules (arrowheads) in the endoA2-depletion condition. The western blot documents the efficiency of endoA2 depletion. Clathin heavy chain (CHC) was used as a loading control. **b**, **c**, Characterization of STxB conjugates with monofunctionalized nanogold. **b**, HeLa cells were incubated for 45 min at 37 °C in the indicated conditions, fixed, treated for silver enhancement, and viewed by transmission light microscopy. Note the strong perinuclear signal (arrowheads) that was visible only when cells were incubated with nanogold-coupled STxB (113 images). **c**, HeLa cells were incubated for 45 min at 37 °C with nanogold-coupled STxB, fixed, treated for silver enhancement, and viewed by electron microscopy after sectioning (32 images). Note the strong signal in the Golgi region (G), which validated the functionality of the conjugate. Some STxB-nanogold could still be seen at the plasma membrane (PM) and in endosomes (E). N, nucleus. **d**, HeLa cells were transfected with negative control siRNAs, or siRNAs against endoA2, incubated for 30 min on ice with nanogold-coupled STxB, shifted for 5 min to 37 °C, and then fixed. Silver enhancement was used to enlarge nanogold particles. Note that STxB-containing invaginations (arrowheads) were much longer in endoA2-depleted cells than in cells transfected with negative control siRNA. Quantification is shown in Fig. 2b (see legend for cell numbers). Scale bars, 10 μm (**a**, **b**), 200 nm (**c**), 100 nm (**d**).

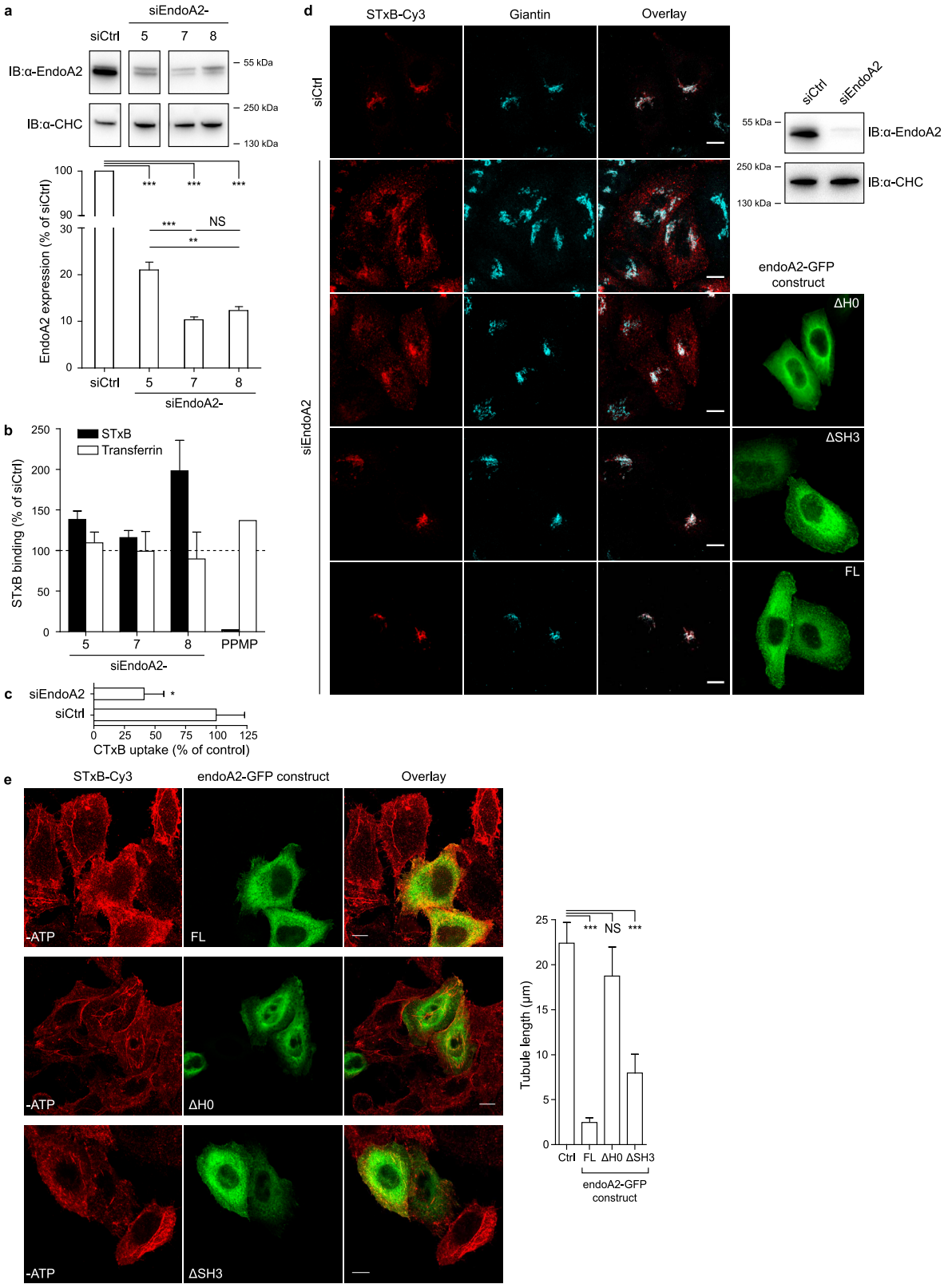

**Extended Data Figure 4 | Effect of endoA2 depletion on STxB and CTxB uptake, and rescue with endoA2 mutants.** **a**, Efficiency of endoA2 depletion with different siRNA sequences. HeLa cells were transfected with three different siRNA sequences against human endoA2 (5, 7 and 8). The efficiency of endoA2 depletion was monitored by western blotting with antibodies against endoA2. Cells transfected with negative control siRNA were used for comparison. The western signal for CHC served as loading control. Quantification shows mean ± s.e.m.; three independent experiments. NS, non significant; $^{**}P < 0.01$, $^{***}P < 0.001$ (Bonferroni's multiple comparison test). Trafficking studies on these cells are reported in Fig. 2c. **b**, Effect of endoA2 depletion on STxB binding to cells. HeLa cells were transfected with siRNAs as in **a**, detached, incubated for 30 min on ice with 1 μM STxB-Alexa488 and 10 μg ml$^{-1}$ Tf-Alexa647, washed and analysed by FACS. Cells treated with the glycosylceramide synthase inhibitor PPMP were used as a control for signal specificity. Mean ± s.e.m. of three independent experiments are shown (except for PPMP, which was done twice). The increased STxB binding with siRNA 8 is not explained at this stage. These cell surface binding data serve as controls for the sulfation experiment of Fig. 2c. **c**, EndoA2 functions in CTxB uptake. CTxB (5 nM) uptake assay (three independent experiments) after 10 min at 37 °C in conditions of endoA2 depletion. $^{*}P < 0.05$ (two-tailed *t*-test). As opposed to STxB, CTxB could be removed from the plasma membrane by acid washes, and endocytosis could therefore be measured directly using a plate-reader assay (see Supplementary Methods). **d**, STxB trafficking rescue experiment under endoA2-depletion conditions. HeLa cells were transfected with negative control siRNAs, or siRNAs against endoA2. After 48 h, endoA2-depleted cells were transfected for 24 h with siRNA-resistant expression vectors encoding: GFP-tagged H0 helix deletion mutant (endoA2ΔH0–GFP or ΔH0), SH3 domain deletion mutant (endoA2ΔSH3–GFP or ΔSH3), or full-length GFP-tagged wild-type endoA2 (FL). STxB–Cy3 (50 nM, red) was incubated with these cells for 45 min at 37 °C (for quantification and statistical data, see Fig. 2d). The H0 helix deletion mutant did not rescue STxB transport to perinuclear Golgi/TGN membranes, as opposed to wild-type endoA2 and endoA2ΔSH3. The western blot documents the efficiency of endoA2 depletion in siRNA-transfected cells. CHC was used as a loading control. **e**, Effect of endoA2 mutants on STxB-induced membrane invaginations. Non-transfected HeLa cells (ctrl) or cells expressing full-length endoA2 (FL), H0 helix deletion mutant (ΔH0), or SH3 domain deletion mutant (ΔSH3) were ATP-depleted and incubated for 10 min at 37 °C with 0.5 μM STxB–Cy3. Tubule length was quantified (control, $n = 277$ in 102 cells; full-length, $n = 90$ in 15 cells; ΔH0, $n = 183$ in 48 cells; ΔSH3, $n = 164$ in 36 cells); two independent experiments. Quantifications show mean ± s.e.m. $^{***}P < 0.001$ (Bonferroni's multiple comparison test). Scale bars, 10 μm.

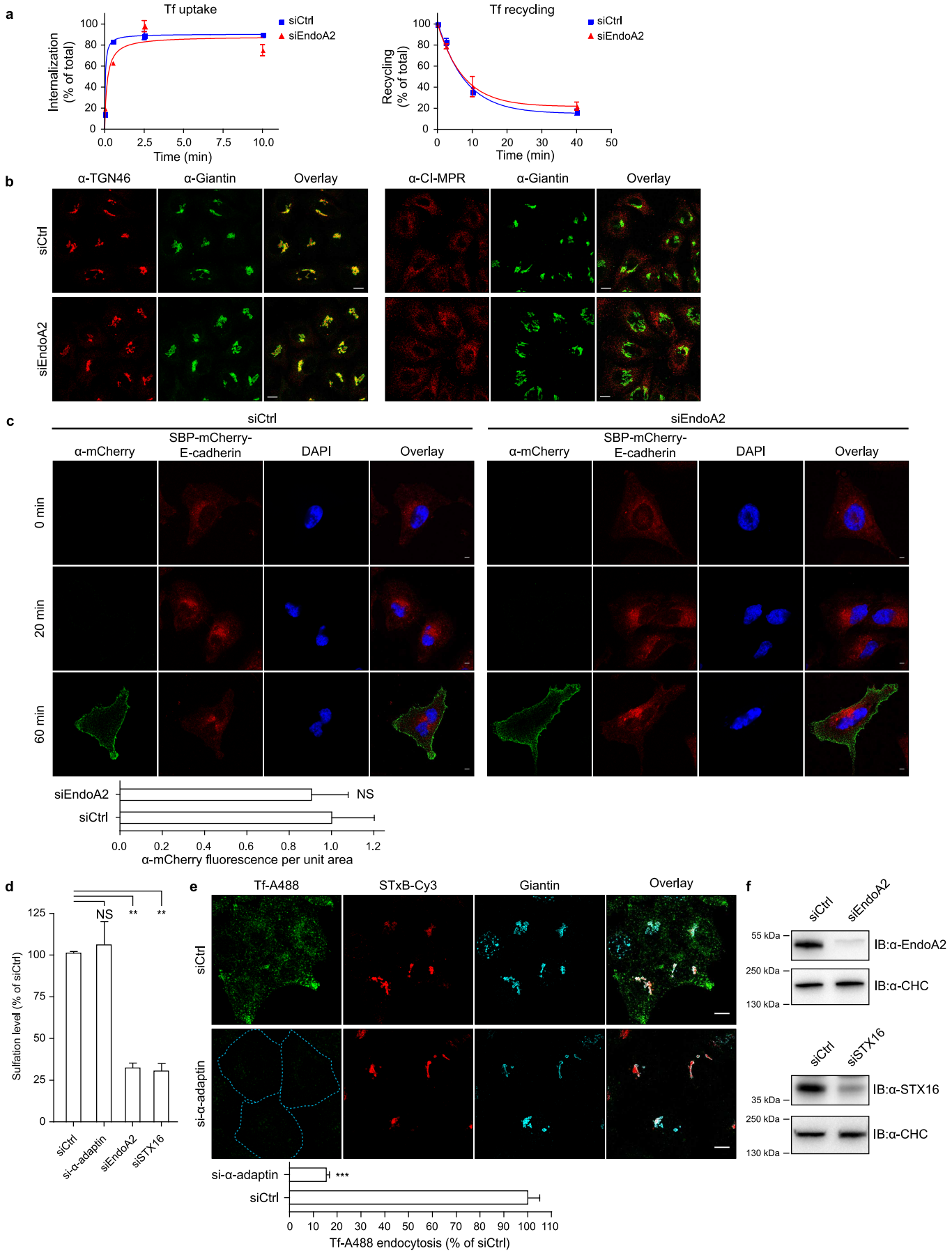

**Extended Data Figure 5 | Intracellular trafficking analysis.** **a–c**, EndoA2 depletion does not affect general trafficking processes. All experiments were performed on cells transfected with negative control siRNAs, and cells that were depleted for endoA2. **a**, Transferrin uptake (left, $n = 3$) and recycling (right, $n = 4$). EndoA2 depletion did not affect any of these processes. Quantifications show mean ± s.e.m. of the indicated numbers of independent experiments. **b**, Steady-state localization of TGN46 and CI-MPR (red), as analysed by immunofluorescence. Golgi membranes were labelled with antibodies against giantin (green). EndoA2 depletion did not affect the steady-state localization of these markers (TGN46 in siCtrl or siEndoA2 cells: 12 images; CI-MPR in siCtrl or siEndoA2 cells: 10 images; two independent experiments). **c**, Anterograde trafficking of E-cadherin. After release from endoplasmic reticulum, SBP-mCherry-E-cadherin protein was detected at the cell surface with anti-mCherry antibodies (0, 20 and 60 min time points). After 60 min, the relative means (±s.e.m.) of anti-mCherry fluorescence per unit area were quantified for control (6 images, 87 cells) and endoA2-depleted cells (6 images, 81 cells); three independent experiments. No significant difference was observed using a two-tailed *t*-test ($P > 0.05$). **d–f**, Depletion of α-adaptin does not affect Shiga toxin trafficking. All experiments were performed on negative control siRNA-transfected cells, and on cells that were depleted for the indicated proteins. Quantifications show mean ± s.e.m. **d**, Sulfation analysis of retrograde STxB transport (three independent experiments). HeLa cells in the indicated conditions were incubated for 20 min at 37 °C with STxB-$Sulf_2$ in the presence of radioactive sulphate, and sulfated STxB-$Sulf_2$ was measured by autoradiography. Note that α-adaptin depletion did not affect sulfation of STxB-$Sulf_2$, whereas depletion of endoA2 or syntaxin-16 had a strong effect. NS, non significant; $^{**}P < 0.01$ (Bonferroni's multiple comparison test). **e**, Immunofluorescence analysis. HeLa cells in the indicated conditions were incubated for 45 min at 37 °C with 0.05 μM STxB–Cy3 (red). During the last 10 min, 10 μg ml$^{-1}$ Tf-Alexa488 (green) were added in the growth medium. Cells were placed on ice, and cell-surface-exposed transferrin was removed by acid washes. After fixation, cells were labelled for giantin (blue). Note that α-adaptin depletion strongly inhibited transferrin uptake, but not retrograde transport of STxB to TGN/Golgi membranes. Transferrin uptake was quantified for control (5 images, 102 cells) and α-adaptin-depleted cells (5 images, 108 cells); two independent experiments. $^{***}P < 0.001$ (two-tailed *t*-test). **f**, siRNA-mediated depletion of endoA2 and of syntaxin-16 was analysed by western blotting. CHC was used as loading control. Scale bars, 10 μm.

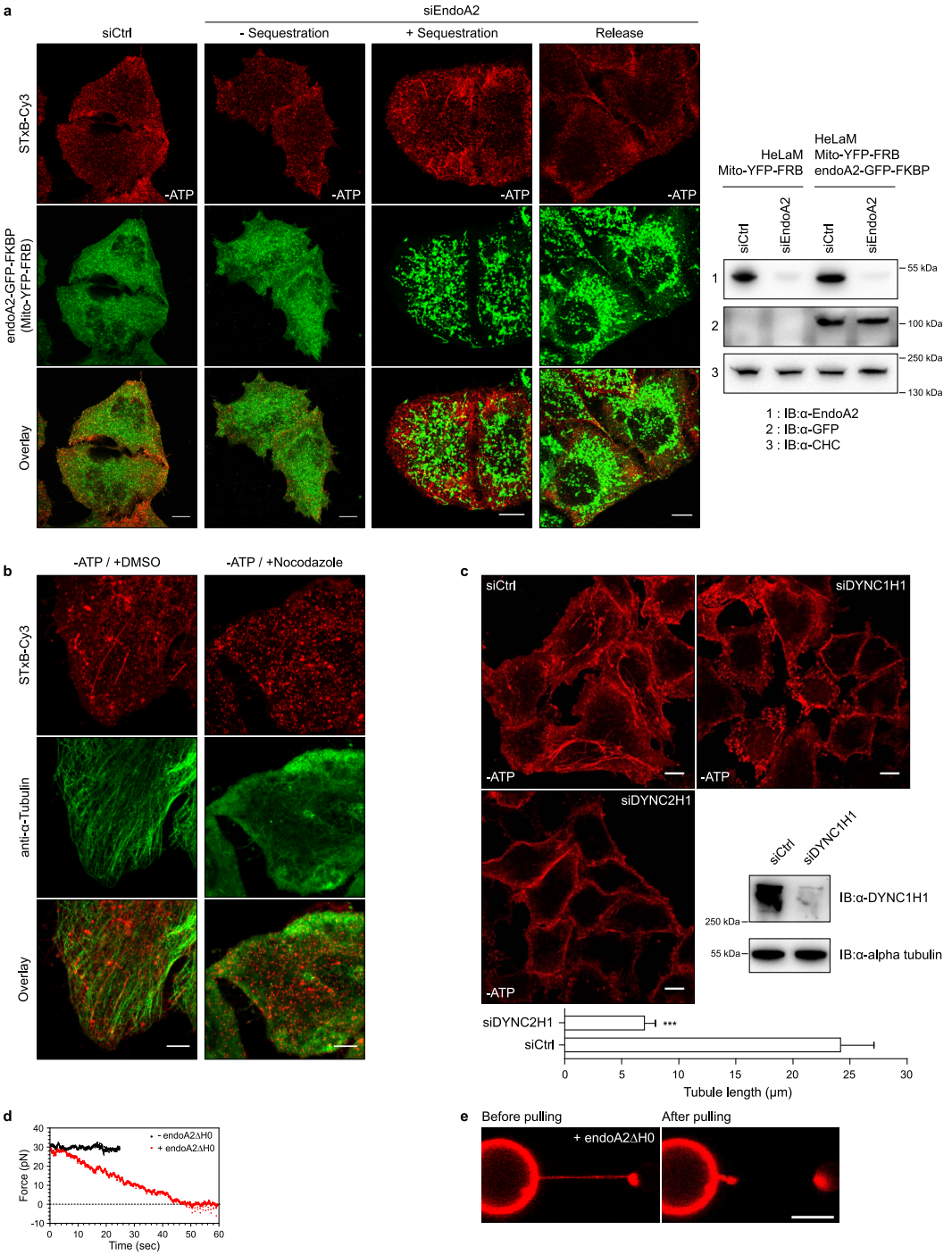


**Extended Data Figure 6 | Cell and model membrane experiments.** **a**, Knocksideways. HeLaM cells stably expressing Mito–YFP–FRB and rat endoA2–GFP–FKBP (green) were transfected with negative control siRNAs (siCtrl), or siRNAs against human endoA2 (siEndoA2) that did not cross with the rat sequence. STxB–Cy3 (0.5 μM, red) was incubated for 15 min at 37 °C with ATP-depleted cells. The cells were then fixed at 37 °C, and viewed by confocal microscopy. Quantification of tubule formation and cell numbers are shown in Fig. 3a. Note that STxB-induced tubule length reversibly increased after endoA2–GFP–FKBP sequestration. The depletion of endogenous human endoA2, and the expression of GFP-FKBP-tagged rat endoA2 were assessed by western blotting with anti-endoA2 and anti-GFP antibodies, respectively. Western blotting against CHC was used as loading control. **b**, **c**, Interfering with microtubules or dynein motors strongly affects STxB-induced tubule length. **b**, HeLa cells were incubated for 1 h at 37 °C with DMSO or 10 μM nocodazole, ATP-depleted for 20 min, and then incubated for 10 min at 37 °C with 0.5 μM STxB–Cy3 (red) in the same conditions. Labelling with an antibody against α-tubulin (green) was used to visualize the efficiency of nocodazole treatment. Long tubular structures containing STxB could not be detected after incubation with nocodazole (−ATP/+DMSO: 18 images; −ATP/+nocodazole: 16 images; three independent experiments). **c**, Heavy chains of cytoplasmic dyneins (DYNC1H1 and DYNC2H1) were depleted from HeLa cells with siRNAs. Cells were ATP-depleted and then incubated for 10 min at 37 °C with 0.5 μM STxB–Cy3 (red). The presence of long STxB-induced tubules was strongly decreased under these conditions. Tubule length was quantified for negative-control-siRNA-treated cells (siCtrl, $n = 188$ tubules in 74 cells) and for DYNC2H1-depleted cells (siDYNC2H1, $n = 165$ tubules in 60 cells); two independent experiments. Quantifications show means ± SEM. $***P < 0.001$, two-tailed Mann–Whitney $U$ test. The western blot documents the efficiency of DYNC1H1 depletion. α-tubulin was used as a loading control. **d**, **e**, Model membranes experiments. **d**, Measurement of tube pulling force over time in the absence or presence of endoA2ΔH0 mutant (7 μM in injection pipette). Representative of six experiments. **e**, Scission experiments with tethers that were coated with endoA2ΔH0 ($n = 5$). Scale bars,10 μm (**a**, **c**) and 5 μm (**b**, **e**).

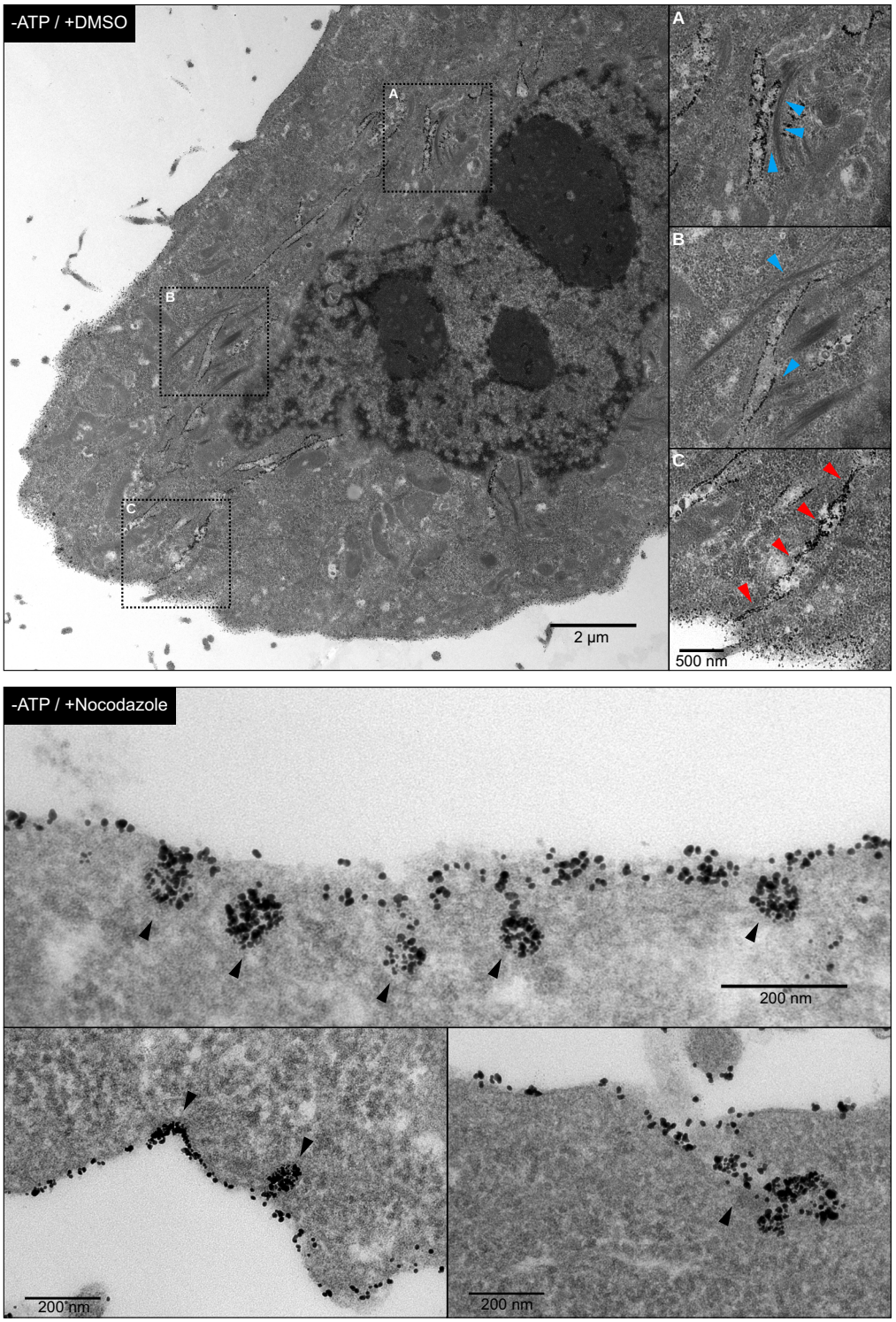


**Extended Data Figure 7 | Electron microscopy of STxB-nanogold on ATP-depleted cells following treatment with nocodazole.** HeLa cells were treated for 1 h at 37 °C with DMSO (top) or 10 µM nocodazole (bottom). During the last 20 min, ATP was depleted. Cells were then incubated for 10 min with STxB-nanogold in the continued presence of inhibitors, fixed, and prepared for electron microscopy. In the DMSO condition (top), long tubular structures connected to the cell surface were observed (magnified views in right insets, red arrowheads in C), as expected from light microscopy experiments. These structures were in close proximity with cytoskeletal elements, as indicated with blue arrowheads in magnifications A and B. In the nocodazole condition (bottom), STxB-induced plasma membrane invaginations were still present (arrowheads), but much shorter (mean length of 118.2 ± 7.0 nm, $n = 109$ invaginations; 0.90 ± 0.12 invaginations/µm of plasma membrane, $n = 28$ images; three independent experiments) than in the absence of the compound. Scale bar sizes are indicated.

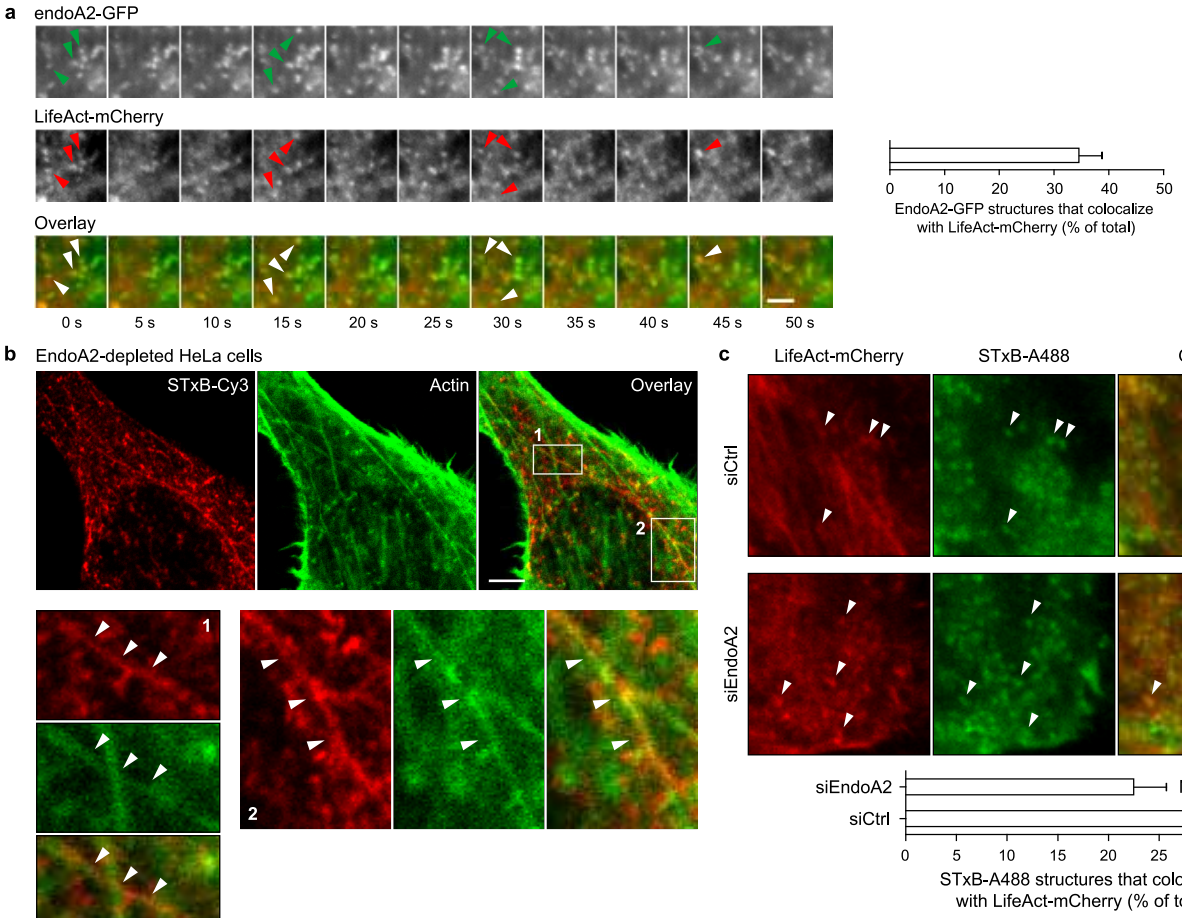

**Extended Data Figure 8 | Actin and endoA2.** **a**–**c**, EndoA2 codistribution with actin. **a**, HeLa cells transiently co-expressing endoA2-GFP and LifeAct-mCherry were observed by time-resolved TIRF microscopy. The panel shows acquisitions at the plasma membrane that were taken at 5-s intervals. Arrowheads point out examples of structures on which endoA2 and actin colocalize in a dynamic manner. Quantification of colocalization of endoA2-positive structures with LifeAct is presented as mean ± s.e.m. ($n = 7$ cells, 2 independent experiments). **b**, EndoA2-depleted HeLa cells were incubated continuously for 5 min at 37 °C with 0.5 μM STxB–Cy3. After fixation, actin filaments were stained with phalloidin-FITC. Arrowheads indicate STxB-induced tubules that are decorated by actin. **c**, HeLa cells transfected with negative control or endoA2 siRNAs and transiently expressing LifeAct-mCherry were observed by TIRF microscopy after addition of 0.5 μM STxB–Cy3 at 37 °C. Arrowheads point out examples of structures on which STxB and actin colocalize. Quantification of colocalization of STxB-positive structures with LifeAct is presented as means ± s.e.m. ($n = 6$ cells, two independent experiments). NS, non significant (two-tailed $t$-test). **d**, **e**, Analysis of STxB-induced plasma membrane invaginations in function of endoA2 depletion and/or actin perturbation. **d**, HeLa cells were transfected with negative control siRNAs or with siRNAs against endoA2, and treated or not with 0.5 μM latrunculin-A. The cells were then incubated continuously for 5 min at 37 °C in the presence of 0.5 μM STxB–Cy3 (red), fixed and labelled with phalloidin (green). The quantification of STxB tubule length is shown in Fig. 4a. Note that tubule length increased with combined treatments (siCtrl+DMSO: 22 images; siEndoA2+DMSO: 11 images; siCtrl+LatA: 14 images; siEndoA2+LatA: 14 images). **e**, Depletion of endoA2 was analysed by western blotting. CHC was used as loading control. **f**, Efficiency of ARPC2 depletion. HeLa cells were transfected for 72 h with a smartpool of four siRNA sequences against ARPC2. The efficiency of ARPC2 depletion was monitored by western blotting with antibodies against ARPC2. The western signal for CHC served as loading control. Corresponds to experiments in Fig. 4a. Scale bars, 2 μm (**a**, **c**), 5 μm (**b**) and 10 μm (**d**).

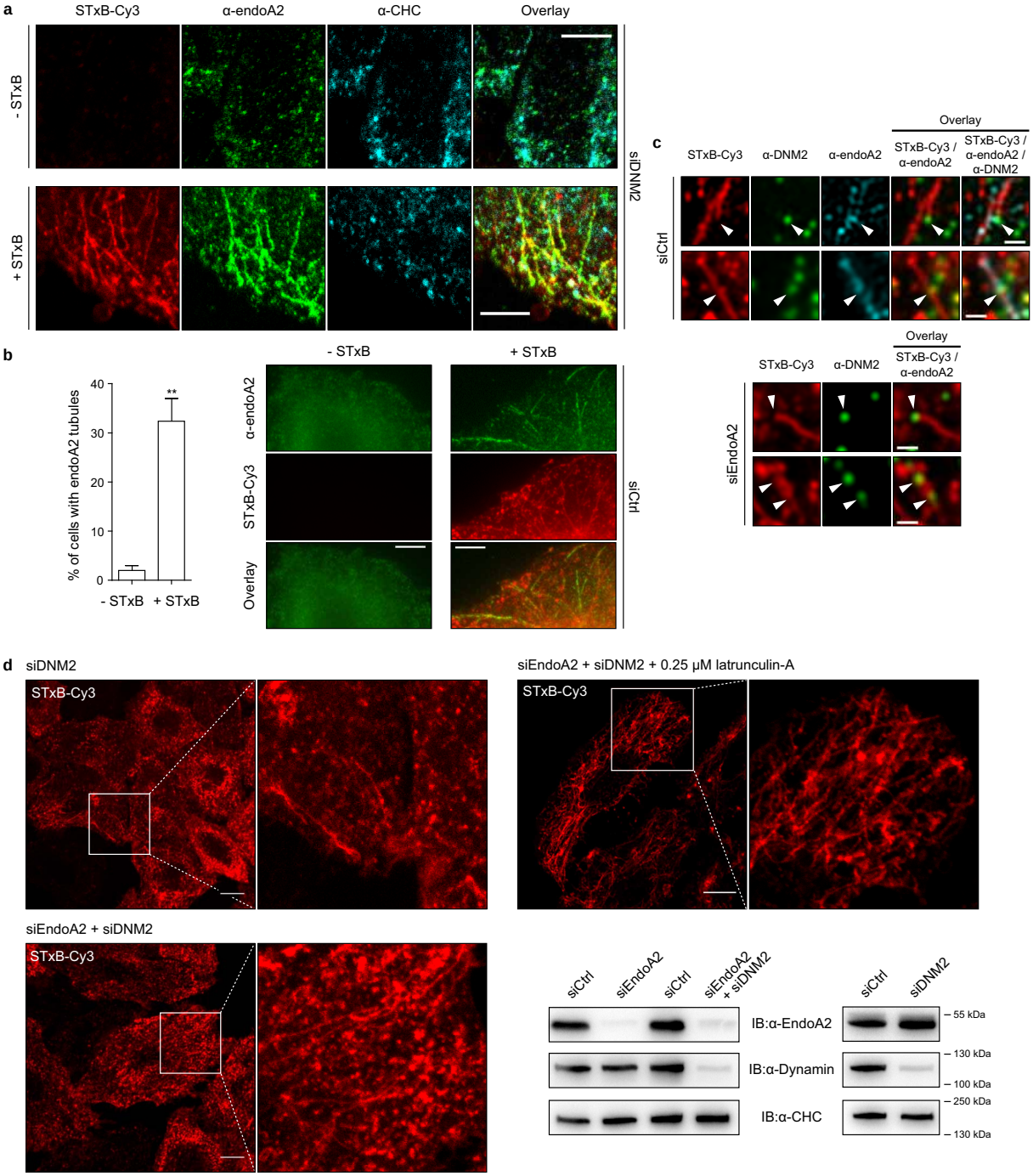


**Extended Data Figure 9 | Combined effects of interference with endoA2, dynamin and actin on STxB-induced membrane invaginations.** **a**–**c**, Endogenous endoA2 and dynamin are found on STxB-induced plasma membrane invaginations. **a**, Dynamin-2 was depleted from cells (siDNM2), which were then incubated continuously for 5 min at 37 °C in the presence or absence of 0.5 μM STxB–Cy3 (red), fixed, labelled for the indicated markers, and analysed by confocal microscopy. Note that endoA2-containing tubules (green) were seen only in the presence of STxB. No overlap was observed with clathrin (blue). –STxB: representative of 15 images; +STxB: representative of 35 images; two independent experiments. **b**, Experiment as in **a** on wild-type cells that were analysed by wide field microscopy. As above, endoA2 (green) was found on tubular structures only in the presence of STxB (red). The quantification shows mean ± s.e.m. of 3 independent experiments on 234 cells without STxB (−STxB) and 921 cells with STxB (+STxB). $^{**}P < 0.01$, two-tailed *t*-test. **c**, Negative control siRNA transfected HeLa cells and endoA2-depleted cells were incubated for 5 min at 37 °C in the presence of 0.5 μM STxB–Cy3 (red). Endogenous endoA2 (blue) and dynamin (green, arrowheads) were labelled with specific antibodies, detected by immunofluorescence, and viewed by structured illumination microscopy. Note that dynamin localized in spots on STxB-induced invaginations, while endoA2 distributed in a continuous manner. **d**, Analysis of STxB-induced plasma membrane invaginations in function of endoA2 and dynamin-2 depletion, and actin perturbation. HeLa cells were depleted for dynamin-2 alone, dynamin-2 in combination with endoA2, or both depletions in combination with 0.25 μM latrunculin-A treatment, as indicated. These cells were then incubated continuously for 5 min at 37 °C with 0.5 μM STxB–Cy3 (red), fixed at 37 °C, and viewed by confocal microscopy. Note that the tubulation phenotype increased with each additional interference modality (siDNM2: 21 images; siEndoA2+siDNM2: 15 images; siEndoA2+siDNM2+LatA: 16 images; two independent experiments). The quantification of tubule length in the different experimental conditions of this figure is shown in Fig. 4a. The depletion of dynamin-2 and endoA2 was validated by immunoblotting. CHC was used as loading control. Scale bars, 5 μm (**a**, **b**), 0.5 μm (**c**) and 10 μm (**d**).

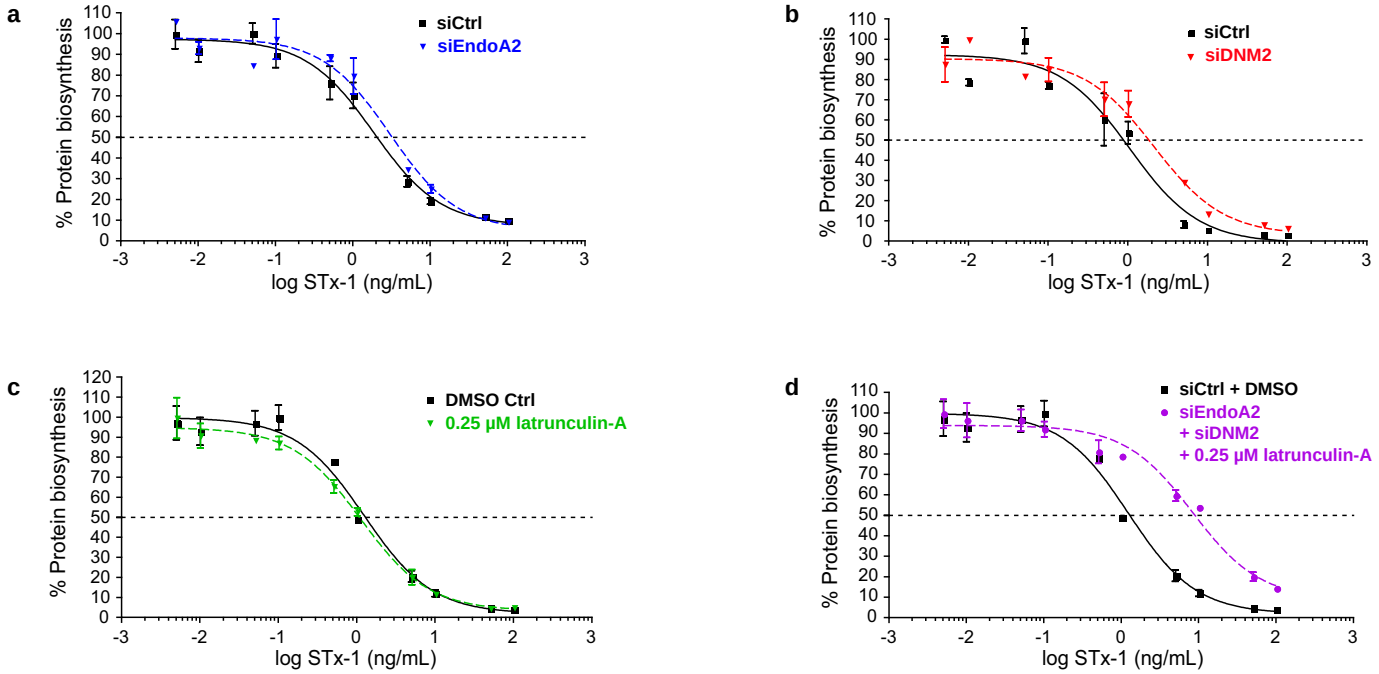


**Extended Data Figure 10 | Intoxication curves. a–d**, HeLa cells were depleted for endoA2 (**a**), dynamin-2 (**b**), incubated with 0.25 µM latrunculin-A (**c**), or submitted concomitantly to all three perturbations (**d**). These cells were then further incubated for 1 h in the presence of increasing concentrations of STx-1, at the end of which protein biosynthesis was measured. Note that only the triple treatment condition had a strong effect on cell intoxication. The protection factors determined on 4–13 independent experiments are shown in Fig. 4c. siEndoA2, $n = 7$; siDNM2, $n = 4$; latrunculin-A, $n = 13$; triple, $n = 4$. Error bars show the s.e.m.